Miniaturised low power IR optical sensor system for high accuracy and high speed identification of linear displacement

Siddiqui, A.

Award date:
2018

Miniaturised low power IR optical sensor system for high accuracy and high speed identification of linear displacement

by

Asim Siddiqui

Department of Mathematics and Computer Science

Eindhoven University of Technology, Eindhoven, The Netherlands

September, 2018

Thesis committee:

dr. ir. S. Stuijk	TU Eindhoven, Supervisor
dr. ir. P.J.A. Harpe	TU Eindhoven
ir. J. A. Huisken	TU Eindhoven, Supervisor
ir. E. G. Veltman	Philips, External Supervisor

This dissertation is submitted for the degree of
Master of Science in Embedded Systems
at
Eindhoven University of Technology,
Eindhoven, The Netherlands.

I would like to dedicate this thesis to my loving parents, my family and friends, the professors at Technical University Eindhoven, Indian Institute of Technology - Delhi, and Jamia Millia Islamia University, Delhi, who helped me achieve my dreams ...

Declaration

I hereby declare that this thesis is my original work as a student at Technical University Eindhoven, Eindhoven, Netherlands while working at Philips Consumer Lifestyle B.V Netherlands during my Masters thesis.

Parts of the thesis where inspiration/content/data has been taken from other work/ research is accompanied by specific reference(s) to the work of others. The contents of this dissertation are original and have not been submitted in whole or in part for consideration for any other degree or qualification in this, or any other university or research publications. I have acknowledged all main sources of help. I solely by myself developed software codes and electronics hardware designs, conducted all experiments, data analysis and interpretation of my results. This dissertation is my own work and contains nothing which is the outcome of work done in collaboration with others, except as specified in the text and Acknowledgements.

Asim Siddiqui
September 2018

Acknowledgements

I would like to extend my sincere thanks to my university supervisors dr. ir. S. Stuijk and ir. J. A. Huisken at Eindhoven University of Technology (TU/e) for their continuous support throughout the graduation thesis phase. They have been available right from day one to immediately assist me and provide me guidance as and when required with their immense knowledge.

I would also like to extend my heart felt gratitude to my external supervisors ir. E. G. Veltman and ir. W. Markenstein at Philips Consumer Lifestyle Netherlands for doing everything possible to provide me with whatever I required. Their feedback and technical know-how was critical in spotting potential errors and suggesting a course correction whenever necessary in a timely manner, yet, giving me complete autonomy to do things my way.

I would also like to thanks the team at Philips with special mention of Peter Viet, Piet Marinus, Sara Delgado, Sewgobind Ruben, Freek Bosker, Mahentesh Bhoomaraddi Appie de Lange and Joop Hendriks. Due to the inter disciplinary nature of my task, the assistance and collaboration extended by all the above mentioned persons have made my thesis possible.

It was indeed a pleasure to work under the guidance of one of the best teachers and engineering teams.

Last, but not the least, I express my gratitude to my parents, family and friends back in India for their continued support, encouragement and belief in me, and for letting me be away from them for 2 long years .....

Abstract

Shaving is a daily activity for most men. Shaving with existing methods such as a shaving blade or an electric shaver tends to cause razor burns or irritation by also cutting the skin at the microscopic level. For electric shavers, there is a precise balance between the closeness of the shave and when the blades start to cut the skin that domes through the cutter cap. In this thesis a method is proposed to better sense the cutting dynamics of the blade inside the rotating shaving cutter in soft real-time. Being able to successfully acquire/sense this data first hand will be the first step to understand how to further improve the shaving process. This is also a first attempt to develop a standalone integrated system with infra red sensors and perform all data and signal processing onboard in a very space and power constrained environment. Since this is the first attempt to develop such a system inside the shaver, my design would be the initial reference standard for any future improvements of the design and also to identify required boundary conditions for the system specification such as accuracy, resolution, tolerances, power consumption etc.

A miniaturised sensor setup has been designed and developed to monitor the cutting dynamics of blades in a shaver head rotating at 2100 rounds per minute using optical measurement techniques. This miniature sensor is capable of measuring distance with an accuracy of about 10 microns. This sensor assembly is incorporated in a very compact space constrained designed within $2cm^2$ and is capable of performing the signal conditioning and signal processing on board in soft real-time. This thesis offers a design approach to measure linear displacement by computing change in intensity of received IR signal after reflection from the surface being measured. Experiments have been conducted to validate the effectiveness of the design, measurement and power consumption. This sensor integration into the design will enrich the understanding of the mechanics of cutting by providing first hand data that has never been acquired before and provide empirical evidence to validate designs and improve them.

Table of contents

List of figures

List of tables

Chapter 1

Introduction

Testing of preproduction design is both an industry standard as well as a vital part of any design or manufacturing process. It is done not only to characterize the intended functionalities/properties of the design but also to validate it before the final production. This ensures technological evolution towards better design and in turn guarantees cost savings and design superiority. High-tech industry involved in development of high precision machining is always in need of better testing methodologies and equipment for micro and nano precision measurements [1]. Very often no off-the-shelf test equipment is available, this results in either ordering for specialised testing equipment which is not only very expensive but also equally time consuming. This has forced several industry leaders and major research & development focused companies to look at developing in-house solutions, custom tailored for their specific high-tech system needs for high precision. This thesis is also the result of one such specialised need for development of in-house testing and measurement technique at Philips Consumer Lifestyle, Drachten, Netherlands.

The male grooming electronics and software engineering department at Philips Drachten focuses on one such high precision engineering task, i.e. development of the best of electric shavers to maintain its market leadership and delivering the best quality products. This market superiority can be maintained by better testing and design, especially for shaver blades and cap, as these shaver blades and caps are designed to give very close yet comfortable shave to the consumer and greatly contribute to consumer satisfaction and consumer retention.

The recent technological developments in Very Large Scale Integration (VLSI) technology have opened new vistas of opportunity and inspired better testing with

on-board sensors for diagnostics and feedback. As the scale of VLSI has increased in recent years, the cost and area required to incorporate electronics in designs has decreased and computation power per unit area has drastically increased [2]. This has enabled integration of miniaturized electronics and sensors at places not deemed feasible earlier. As a rebound effect, this has had a profound impact on deepening the appreciation of sensors and embedded intelligence in all aspects of technology, especially consumer electronics, since consumer electronics are more focused on industrial design, size and cost [3]. Integration of sensors also provides unprecedented opportunities for user experience improvement, quality improvement, preventive maintenance, reduced mean time to repair, better development and testing. Sensor integration coupled with unceasing electronics miniaturization has made it possible to produce inexpensive sensing electronics in everyday devices [4]. One of the application areas is use of sensors in high precision sensing and measurement.

For Philips, it's an opportunity to gain a better insight into the dynamics of the electric shaver's cutting blades and cap while the system is in operation, it is desired to move forward to developing a better miniaturised platform with micrometre resolution that is not hindered by the size constraints and is able to capture the details while the shaver cutter system is in operation. To do so, the sensing electronics needs to be miniaturised enough to fit inside the very small space constrained shaver cap and blade assembly with minimal change to the existing design.

Thus, the focus of this thesis is to incorporate a standalone sensing and measuring system within the rotating shaver head to measure the cutting dynamics with micrometer(μm) accuracy while the shaver is in operation. This will enable the design and testing teams to make measurements and validate designs while the shaver is in operation for the very first time. This was until now not possible with the present in-house testing equipment such as Optical Coherent Tomography (OCT). The developed miniaturised sensing system will be installed on a very small and space constrained cutter head. All the signal conditioning and processing of the IR sensor will be performed on board and processed information will be delivered to a computer for visualization.

1.1 Background

The sales of conventional cartridge shavers or disposable shavers has plummeting drastically across developed world. The major market share is engulfed by the consumer switching to electric shavers. This has slingshot the global electric shaver market to more than US$ 14 Billion in 2017 [5].

With the coming of smart and connected devices in the consumer market, the user expects to get a more personalised and connected smart device for all everyday use consumer products. Electric shavers happen to be one of them. With rising economies, the consumers have more disposable income. This has in turn increased the possibility for electric shaver companies to add more futuristic functionalities into the shavers. This includes creating internet-of-things (IoT) connected devices, personalised experience as well as more sensors that add to the functionality and comfort of the device and consumer respectively.

In order to speed up the development and testing of these cutter and caps, presently optical coherent tomography (OCT) is used . This is a non-destructive, non-invasive, non-contact optical based technique used at Philips to inspect the developed mechanical designs of the cutter and cap. Here coherent light is used to capture micrometre resolution images of the surface morphology. The equipment used to perform such kind of testing is expensive and bulky and can't perform the surface morphology and measure the amount of skin coming inside the shaving cap in soft real-time while the shaver is being used. Moreover even this measurement using OCT is possible only for a few shaving cap slots/holes at a time . This thesis is an attempt to remove this bottleneck.

1.2 Motivation

There are primarily two main driving forces behind this effort:

1.2.1 Technological Motivation

It is essential to measure the performance of the shaving cap and cutter system with respect to amount of skin doming to verify the adequacy of the shaving assembly design and measure excessive skin doming refer section 1.3 below for definitions. Generally, as explained in the previous section optical coherent tomography is used

for skin doming measurement, but due to the principle of operation of OCT machine, the testing process is very slow, costly and time consuming. More over due to the size and operational complexity of the machine, these measurements can't be performed while the shaver is in operation and not all engineers can use it, as, where and when required.

Furthermore, as a result of this thesis, sensor integration will take Philips' male grooming product range one step closer to creating a more personalised shaving experience and IoT connected Philips products.

1.2.2 Better Consumer Experience Motivation

Looking through the lenses of consumer satisfaction and experience, there is presently no feedback system in any of the existing electric shavers in the market to prompt the user if he is putting excessive pressure while shaving, thereby exposing the skin to potential razor burns. Being the first to bring such a product in the market adds to the products market superiority and improved customer satisfaction.

The above mentioned are the two main factors that have fuelled this pursuit to develop a miniaturised, cost effective, power efficient sensing system that can measure the amount of skin doming from inside the shaving cutter in soft-real time with micrometre accuracy.

1.3 Nomenclature

This section defines the technical nomenclature that would be used in the thesis to refer to the parts of the shaver assembly. The technical nomenclature is same as the one used in the mechanical design documentation.

1.3.1 Definitions:

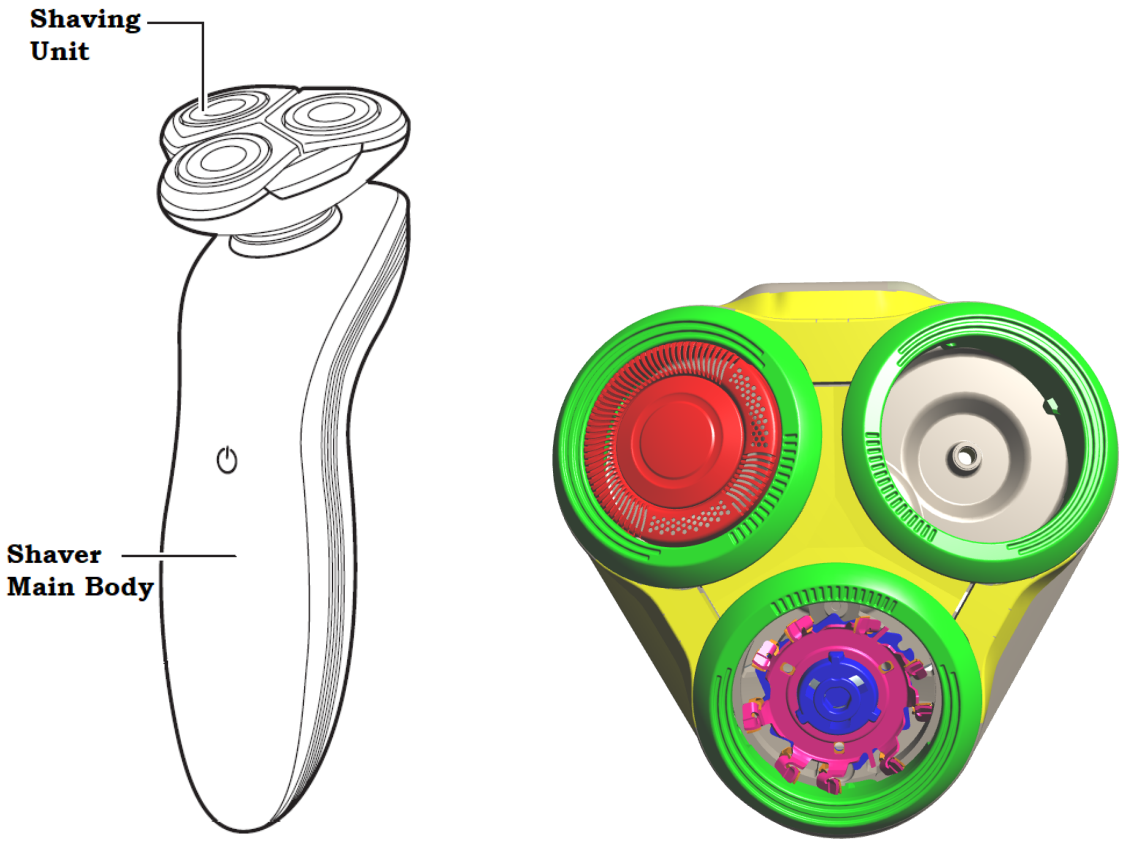

(a) Philips electric shaver

(b) A 3D CAD image for the shaving unit showing its different of parts

Fig. 1.1 Figure (a) shows the complete Philips shaver and (b) shows a 3D image of the shaving unit

Shaver Main Body:

Figure 1.1a shows the overall view of the complete shaver. It primarily comprises of a shaver main body and shaving unit. The shaver main body houses all the control electronics, buttons, rechargeable batteries, motor etc. This is the part of the shaver which the user holds to operate the shaver.

Shaving Unit:

Figure 1.1b also shows the shaving unit, which is a detachable housing that contains the shaving assembly as shown in figure 1.2. The shaving unit contains up to 3 shaving caps each with its own individual shaving assembly.

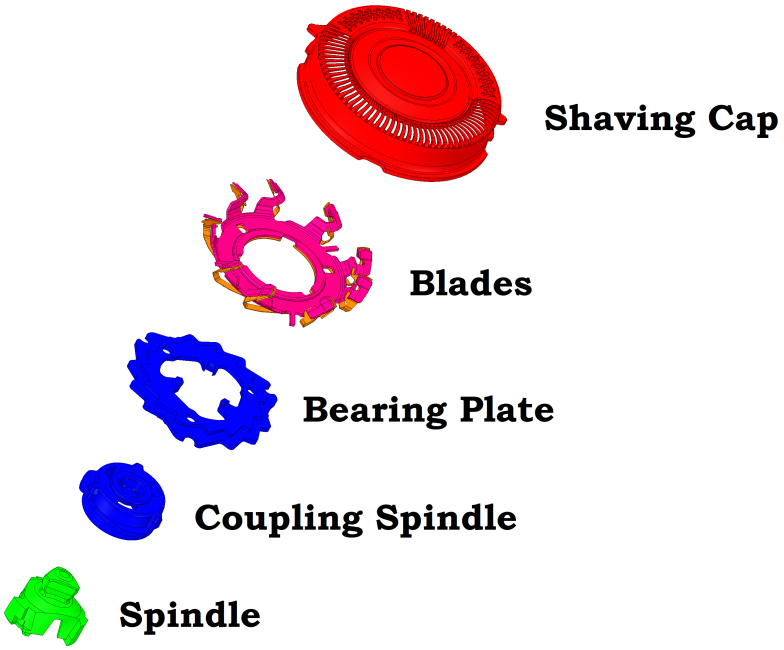

Fig. 1.2 Exploded view of one of the shaver unit cutting systems

Shaving Cap:

The shaving cap is the top most part of the shaving assembly as shown in red in Figure 1.1b and 1.2. It is this part that comes in contact with the hair and skin. As visible from figure 1.3, moving clockwise from the array of 49 full slots and 1 half slot followed by a pattern of 38 holes which is again followed by 9 full slots and 1 half slot and again 38 holes. In total the shaving cap has 58 slots(+2 minislots) and 76 holes.

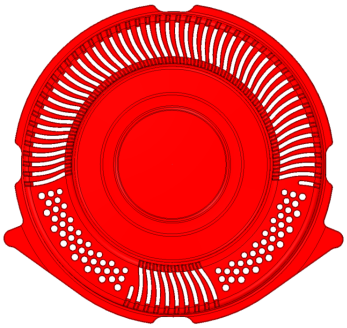

Fig. 1.3 Enlarged view of the shaving cap

The mechanical dimensions and number of the slots and holes is a critical balance between closeness of the shaving and comfort to the user. If the slots/holes are wider it will be easier for the hair to come in and get cut by the rotating blades but at the same time it may also allow too much of the skin to come in through the shaving cap slots and holes and get cut by the rotating blades, causing irritation (razor burn) and redness. If the width of the slots/holes is too less there will be very less skin coming in, which prevents skin being cut but at the cost of a close shave. Also, smaller slots/holes makes less hair come inside the cap which increases the shaving time. Hence the right balance of the dimensions of slots and holes in the cap is critical.

Cutter:

The cutter as shown in pink in figure 1.4, is an arrangement of 9 blades that rotate at 2100(±200) RPM, sliding on the inside of the shaving cap. Anything that comes inside the shaving cap (both hair and skin) is cut by these blades.

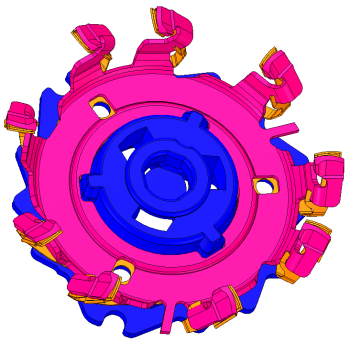

Fig. 1.4 Blades in pink with bearing plate and coupling spindle in blue color

Bearing Plate:

Bearing plate in blue is the base plate that connects the cutter with the coupling spindle.

Coupling Spindle:

It is the mating point for the shaving unit and the spindle which is a part of the main shaver body. It couples the rotational energy of the spindle to the shaver unit.

Spindle:

The spindle is a part of the main shaver body which provides the rotational energy to the shaver unit.

Skin Doming:

The term skin doming is coined to describe the process of skin protruding through the shaver caps slots and holes to form something resembling a dome shape as shown in figure 1.5. This happens due to excessive pressure being applied by the user while shaving. This is the root cause of razor burns that are caused by this protruding skin being cut by the cutter blades.

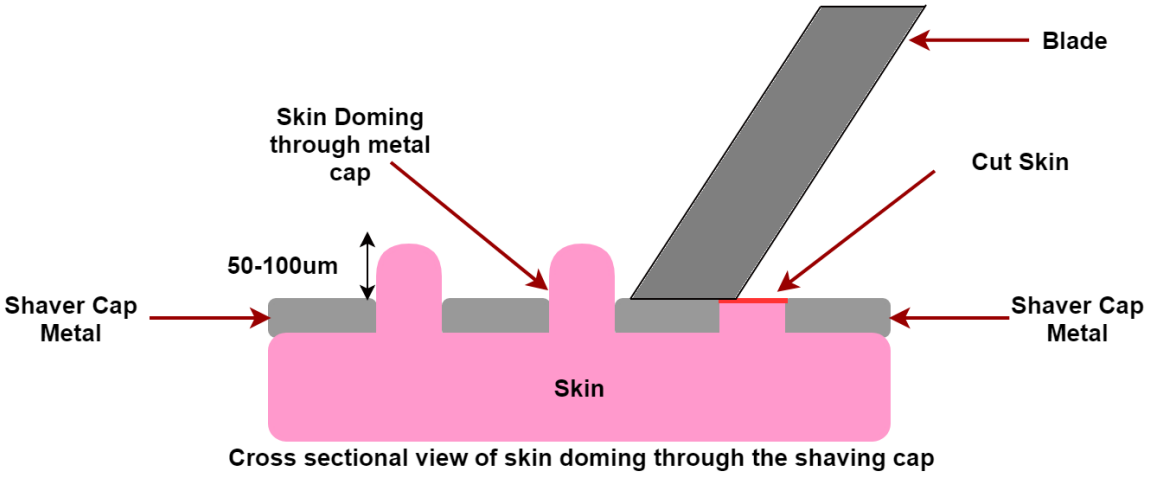

Fig. 1.5 Skin doming visualization of how the skin forms a dome which is then cut off by the blade

1.4 Problem Description

Measurement of linear displacement with micrometre accuracy within a highly space constrained mechanical assembly moving at high speed while maintaining high accuracy at a high response rate with low cost and power consumption is a challenging affair. This thesis is aimed at measuring skin bulging through the shaver cap (termed as skin doming) with an accuracy of few μm through a standalone miniaturised measuring system put inside the cutter.

Application to real world problems: In terms of the real world problem this thesis is aimed to solve the issue of electric shaving cutters cutting the excessive skin that domes or enters the metal shaving cap through the slots and holes, refer figure 1.5 which shows skin doming and its effect in figure 1.6. This is due to the fact that the user has no feedback that he is applying excessive force while shaving which causes the skin to dome and eventually be cut by the rotating blades; this causes skin irritation or razor burns refer figure 1.6.

Fig. 1.6 Red spots on the skin indicate razor burns caused by excessively domed skin being cut by the blades [6].

For test engineers at Philips this thesis would give them the first glimpse into what actually happens to the skin while shaving. As of now all the understanding of engineers is based on simulations, calculations, readings and measurements taken under OCT in stationary condition. This thesis enables them to get near real-time data about the skin doming and cutting dynamics of the shaver at each individual slot.

Design Challenges: What makes the task even more challenging is to design a standalone sensor module with minimal changes in the existing mechanical assembly for easier integration of the sensor system post development into the existing product. The major challenges are to develop an optical sensor system and integrate all electronics and embedded intelligence into the design while maintaining good linear response, high sensitivity and repeatability over time. Further details about the goals and deliverables of this thesis are explained in the following section.

1.5 Goals and Deliverables

This section discusses the design requirements. Each goal section defines the design quantitative deliverables:

1.5.1 Design Goals

The design prototype should meet or exceed the following quantitative and design requirements:

D.1 Design a miniaturised standalone sensor system with on-board signal conditioning and signal processing within an area of about $2cm^2$.

D.2 Design an optical assembly for precise detection of linear displacement(skin doming) which can fit within the shaver cap with minimal changes to the existing assembly.

1.5.2 Measurement Goals

The measurements should include the following:

M.1 The system should be able to measure skin doming with an accuracy of about 10μm.

M.2 The amount of linear displacement (skin doming) should be measurable at each slot of the cap.

M.3 Linear displacement (skin doming) should be measured within 78ms.

1.5.3 Analysis Goals

The analysis should include the following:

A.1 The data should be visualised on a graphical user interface, indicating the amount of skin doming in μm in each slot of the shaver cap.

A.2 Power consumption of sub systems should be analysed and should be within 45mW.

1.5.4 Documentation Goal

The thesis documentation should include the following:

Do.1 Literature survey of existing state of technology

Do.2 Documentation of tests and experimentation such as power consumption, skin doming measurement etc.

Do.3 Software code with flow charts.
Do.4 Power saving techniques and code optimization.
Do.5 Recommendations for further development and optimization of the system

1.6 Organization of Thesis

Chapter 2 Review of Existing State of Technology and Literature

This chapter provides an overview of existing state of technology and literature related to the objectives of the thesis.

Chapter 3 System Level Design

The system level design of the complete sensor system is provided to give the reader a birds eye view of the hardware and software subsystems. This chapter also defines the functionality of each part of the system and parts of the system left for future implementation.

Chapter 4 Sensor and Sensor Assembly

The description of the sensor and its optical assembly is presented in this chapter. Based on the present state of technology, justifications for the sensor properties, design specification, response time and power budgeting is also addressed in this chapter.

Chapter 5 Optical Measuring Platform

The optical measuring platform chapter describes the circuit design of the measuring system which includes the sensor, its signal conditioning and signal processing and associated calculations/circuit diagrams.

Chapter 6 Measurement Algorithm

The measurement algorithm explains in detail the characteristics of the input signal and the functionality of the measuring algorithm. It also discusses the power saving schemes implemented in the algorithm to meet the power consumption requirements of the design.

Chapter 7 Measurements and Analysis

This chapter compiles all the test measurements and results. The results are interpreted and analysed. It also validates if the initial design goals and deliverables are met.

Chapter 8 Conclusion and Future work

This winds up the complete work of the thesis, it draws the conclusion of the work as well as discusses the deficiencies and shortfalls of the proposed design. The chapter ends with discussion of the scope of future work.

Chapter 2

Review of Existing State of Technology and Literature

2.1 Literature Survey

It has been several decades since the idea of using optics as a measuring method was conceived and experimented upon. The possibility of ultrafast sampling and photo conductive switching opened a new domain of sensors capable of measuring with much shorter response time than with purely electrical methods. Optical sensors are not only much faster and non-invasive but recent developments have also drastically improved their measurement resolution by incorporation of different/new scanning techniques [7]. Sensors with a precision of $\pm 1\mu$m are in high demand. But measurement with high precision still remains a challenge in several application areas where the sensor weight and size is constrained while maintaining a linear response with adequate accuracy [8].

Precision can be attained by use of several types of sensors which are broadly classified as contact and non-contact sensors. But for our application non-contact sensors are ideal due to requirements of high-speed measurement, high accuracy, non-contact measurement, immunity to EMI etc. Thus, ideally for this thesis problem statement a non-contact optical sensor is preferred.

2.2 Present State of Technology

In the last decade extensive research has been done into sensors; especially displacement sensors. This has resulted in a manifold increase in performance enhancement

with respect to sensitivity, resolution, compactness, long-term stability, drift, and power efficiency of interface electronics [9]. Advancements in VLSI have lowered cost and energy consumption of sensors and miniaturised interfacing electronics. This has made integration of interface electronics together with sensing elements into smaller and smaller area possible [4],[9] .

In the design proposed in this thesis, it needs to be thought a step ahead because of the future incorporation of a dynamo to make the system truly self-powered. Hence due to the space constraints for the PCB, light weight and the required immunity against noise and electromagnetic interference, only one type of sensor class qualifies for such an assemble i.e an optical sensor [10],[11],[12],[13]. Thus in this thesis an optical based sensor is used to achieve the design goals.

2.2.1 Related Research on Skin Doming

The initial proof of concept of this idea was presented in [14] to measure skin doming using optical fibre cables. But optical fibre based sensing systems are plagued by other inherent deficiencies, such as its polishing and difficult and fragile integration into the design [15]. In addition to the above mentioned constraints and drawbacks, the proof of concept as presented in [14] suffered from bulky measurement system (National Instrument data acquisition unit), high optical coupling losses (at both infrared emitter/receiver), high power consumption due to long fibre lengths and no power optimization algorithm.

Several of the problems with the initial proof of concept design by [14] are overcome in this thesis. But the use of optical fibre cables still remains pivotal in achieving the aim of this thesis despite the given drawbacks. The reason being that fibre optic cables provide a very narrow field of view of the slots of the cap passing over it. Precise and narrow field of view is necessary for the system to measure skin doming at each individual slot/hole of the shaving cap. Achieving this with just the SMD IR emitter and receiver pairs is not possible because of their wide directivity ($\pm$ 70 degrees)[16],[17].

Not using optical fibre cables results in the sensor receiving reflection from several slots instead of just one; thereby defeating the aim of measuring skin doming at each individual slots. Also wide half angles of the receiver and emitter create a lot of reflections from neighbouring surfaces thereby creating a fixed DC offset in the photodiode sensor response. A new design assembly is conceived that uses much smaller

fibre optical cable lengths and provides better optical couplings than initial proof of concept design developed by [14].

2.2.2 Related Research on Energy Harvester

For the dedicated purpose of making the skin doming measuring system passively powered, work has been done to develop prototypes for the energy harvester. Work reported in [18] has investigated different energy harvesting techniques, theoretical models and performance measurements. The maximum power generation reported was about 3mW. Theoritical calculations indicate that an improved iteration of the energy harvester is expected to generate 50mW of power [18].

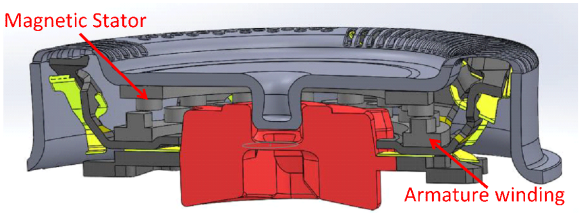

Fig. 2.1 Cross-sectional 3D CAD view of the energy harvester [18].

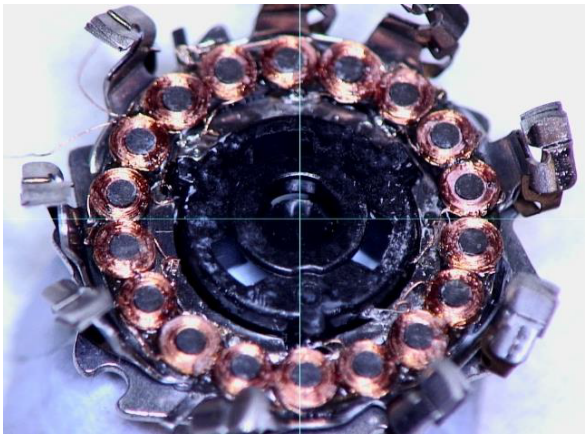

Fig. 2.2 Magnified image of the armature coil on cutter [18].

2.2.3 Related Research in Power Rectification

The AC generated by the energy harvester needs to be rectified to run the on-board electronics. A novel approach to use the body diodes of microcontroller's general

purpose input output (GPIO) pins for rectifier has been investigated [19]. Since the microcontroller uses its own GPIO pins, active rectification has proven to be beneficial and feasible. Initially passive rectification is performed and the microcontroller measures the frequency and phase of the input AC signal, these measurements are later used by the microcontroller to calculate when to switch the GPIO mosfets to perform active rectification. The microcontroller uses the recertified power to run itself as well as perform active rectification to run other peripherals like sensors. Active rectification provides 460% higher DC output power from the energy harvester than passive rectification [19]. As of now using this approach on a generic 8bit microcontroller can actively rectify input AC signal with frequencies upto 1kHz [19].

2.2.4 Measuring Approaches

Recent research has been done using IR emitter receivers which find immense application in todays smart phones. One of these research areas is Dynamic vision sensors (DVS), these are a replication of human optic nerve, and have been found to be very power efficient and fast responding sensors [20]. It outputs time synchronised light for certain time period and measures the reflection coming back if this reflection is above a certain threshold then some inference is derived. But this approach measures aggregated refection of light and fails to differentiate environmental noise[21]. A new method is proposed by researchers at Samsung. This method utilizes time domain analysis. Samsung suggests two main algorithms to estimate proximity of the object using a light source and a DVS. One algorithm estimates distances based on spatial information of the reflection while the other is temporal pattern recognition [21]. This algorithm estimates distance in realtime by detecting the change in brightness and outputs the spatial information of the reflection. As the distance of the object varies the spatial information also varies.

Since the aims of this thesis includes power efficient onboard processing in soft-realtime of the sensor data, literature study has been done on efficient processing of streaming data or post processing of long batches of captured sensor data. Maxlist algorithm is an efficient algorithm to process data by extracting only required data values from a data stream [22]. It identifies the minimum or maximum values across a sliding data window and is less sensitive to data correlations [22], hence more immune to processing uncorrelated data stream. In Maxlist algorithm the sliding window size is fixed , but use of this algorithm with dynamically adjusting window size needs to be explored.

Chapter 3

System Level Design

This chapter gives a system level design of the complete sensor system. The purpose of this chapter is to give a purely external view of the system. Broadly, it shows the major part of the system and in which level of the design it lies in. It delves into relationships between different parts of the system and their intended functionality.

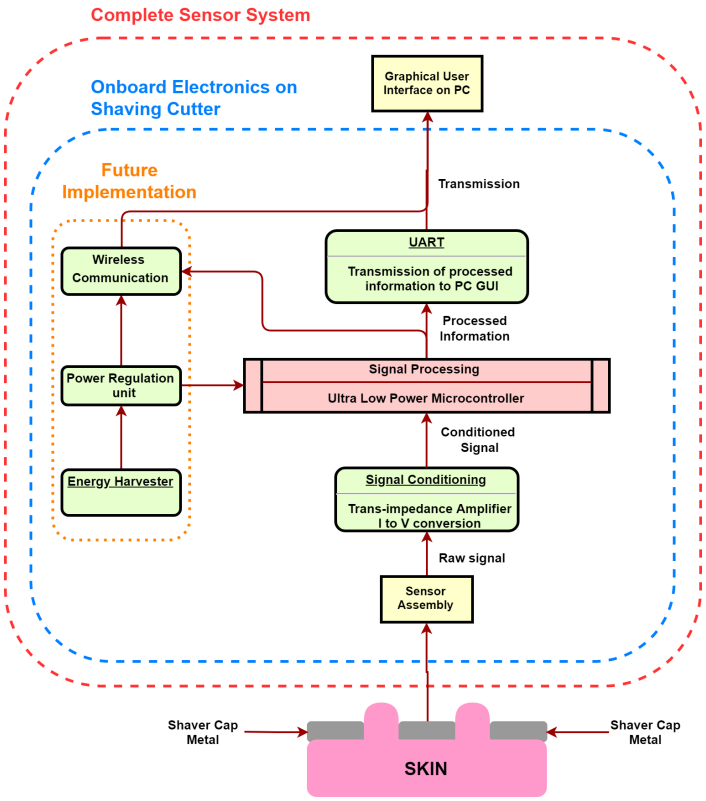

Fig. 3.1 System level design

Figure 3.1 shows the data flow diagram of the system level design. Different colour codings are used to classify different parts of the system.

The red dotted line encompasses everything that is a part of the system. The blue dotted line indicates all modules and processing that is being done on-board the PCB on the shaving blades. Orange dotted lines indicate system parts that are to be developed for future implementation.

The following sections define system level specifications for each part and their intended functionality. We will be using the same nomenclature as in 1.3.

3.1 Sensor Assembly

The sensor assembly includes an Infrared (IR) transmitter , IR receiver (photodiode) and optical wave guides for both the transmitter and receiver. These optical wave guides are fixed in a 3d printed mechanical assembly. Using the waveguides and 3D printed sensor assembly reducing the field of view of the emitter and receiver, mechanical vibrations and optical crosstalk. Refer figure 4.5 for the CAD image of the 3d printed part.

This sensor assembly measures the surface from the inside of the shaver cap. It identifies amount of skin doming by measureing the change in the reflection intensity at the receiver due to skin doming. The sensor assembly gives a raw signal in the form of photocurrent to the signal conditioning unit.

3.2 Signal Conditioning

The raw signal for the sensor assembly is in the form of photocurrent generated by the IR photodiode. This signal needs to be conditioned to make it usable for the next stage of the system. Hence, the signal conditioning unit includes a transimpedance amplifier, which converts the photocurrent to voltage. This voltage is then fed to the next stage in the design i.e the signal processing unit. The signal conditioning unit is discussed in more detail in chapter 5.

3.3 Signal Processing Unit

The microcontroller is the embedded intelligence in the printed circuit board (PCB). The system uses an ultralow power microcontroller; this microcontroller reads the conditioned signal from the signal conditioning unit of the design through an analogue-to-digital converter (ADC). The ADC sampled values are processed via an algorithm running in the microcontroller to convert the received values into equivalent skin doming in microns. Further details about the algorithm are mentioned in chapter 6.

3.4 Universal Asynchronous Receiver-Transmitter (UART)

The UART is the communication channel for communicating the processed information to the PC for visualization. The UART information is transmitted via slip-rings which connect the rotating sensor system to the stationary wires which are connected to an external UART to USB converter. This UART to USB converter finally relays the information to the PC for visualization via USB.

3.5 Graphical User Interface (GUI)

The information about the skin doming is received from the sensor system. The received information is visualised on the PC via a GUI. The GUI will represent skin doming in microns at each individual slot of the shaving cap. Further details about the GUI are explained in chapter 7.

3.6 Energy Harvester

The energy harvester is a dynamo which converts the rotational energy of the cutter to electrical energy. It's a simple generator which is designed to fit in a very space confined area, an initial prototype is shown in figure 2.1 and 2.2. The given image is an earlier design where the dynamo structure is in the front of the shaving cutters, but in future products it will be placed on the back of the cutter system. This is not a part of this thesis but is a part of the sensor system. Details of power extraction from this energy harvester to regulate usable DC voltage is explained in the next section.

3.7 Power Regulation Unit

Section energy harvester explains generation of AC using a dynamo, hence rectification and regulation needs to be done for the system to use this as a power source. Work has already been done on active rectification of the AC signal using a microcontrollers GPIO ports for rectification [19] . This has given very promising results with better conversion efficiency than a bridge rectifier [19], future work will be focused on using the same system hardware and microcontroller for active rectification. Development of the power regulation unit is not a part of this thesis but is intended for future development.

3.8 Wireless Communication

The wireless communication system will be a replacement of the existing UART communication which uses slip-rings to transfer processed data to GUI for visualization. Development of wireless communication is reserved for future and is not a part of this thesis.

Chapter 4

Sensor and Sensor Assembly

The basic principle of optical measurement approach used in this thesis is the measurement of change in the received light intensity after reflection. This is one of the simplest approaches with most optical sensors. In such cases the light intensity modulation of the received light reflected from the tested surface is compared with some known parameters and relations [23]. This comparison or relation yields information about the physical quantity being measured by the sensor .

In this thesis an optical sensor system is developed that can measure skin doming with and accuracy of nearly $\pm 10\mu$m. The light reflection from the metal cap and due to the skin doming is incident on a photodiode that generates a photo current. A transimpedance amplifier is used to convert this current to voltage with a very high gain since the photo current is of the order of a few micro amperes. After characterization this voltage change is related to measure skin doming with micrometre accuracy.

4.1 Description of Optical Sensor

Although there are various methods to measure the displacement with high precision using non-contact methods such as triangulation-laser displacement sensor [24],[25], Interferometry [26], capacitive sensor [27], magnetic reluctance sensor [28], hall effect sensor [29], but all these techniques have drawbacks such as size, complicated assemble, cost and cumbersome installation [30], [31]. Several factors make the measurement of small linear displacement in compact devices even more complicated, such as minimal mass dimension, high measuring sensitivity and immunity to electromagnetic interference especially due to the compactness of the sensor and measuring system [8]. Furthermore, the optical fibre sensors working on the principles of intensity mod-

ulation have enabled precise positioning [32], [33]. The use of light emitting diodes (LED) distance sensor for high resolution displacement measurement is a cost effective alternative and an inherently safer and smaller alternative to sensor using lasers and optical fibres assemblies [34]. Lastly, due to their light weight, small dimension fibre optic cable (FOC) based sensor have already proven to be ideal for measuring even nanometre displacements and precise positioning [35],[32],[33].

More over while narrowing down to the most ideal sensor for this application we need to look at another design constraint. This system design requirement is to make the whole sensor system passively powered for future developments. Since the cutter assemble rotates at 2100($\pm$200) RPM, hence the most ideal approach towards self-powered design is the use of a dynamo and the only location for the dynamo coils to be placed is behind the electronics assembly, refer fig. 2.2 for an initial prototype for energy harvester [18]. This means that the sensor also needs to be immune to EMI, therefore only one type of sensor within the given design constraints of size, accuracy, sensitivity, response time, cost and EMI immunity was eligible i.e an optical sensor.

Hence to make the system smaller, compact, more sturdy and practical without compromising on the requirement, the measuring system using an optics-based displacement sensor is most meaningful and practical.

4.2 Sensor Wavelength

The design constraints identified at the start of this chapter are considered here while choosing and designing the sensor assembly and circuit. With the aim to comply with the design specifications and requirements several configurations and mechanical assemblies were fabricated and tested, but design assemblies that introduced noise, vibrations, reduced sensitivity, increased optical crosstalk or power consumption were removed. This chapter discusses only that design iteration that succeeded to meet or exceed all design parameters and specifications.

The base assembly of the sensor system consists of an Infra-Red (IR) emitter and IR photodiode (receiver). Both the emitter and the receiver are tuned to operate at 940nm. The reason for choosing a 940nm IR wavelength is the fact that around this wavelength, light is least affected by the human skin colour [36] and is also one of the most commonly available SMD IR emitter and receiver wavelengths in the market.

Thus, operating the sensor in this wavelength will yield same intensity of reflected light for a wide range of skins colours, making it more close to a practical solution. An image of light reflection as a function of skin colour is shown in figure 4.1.

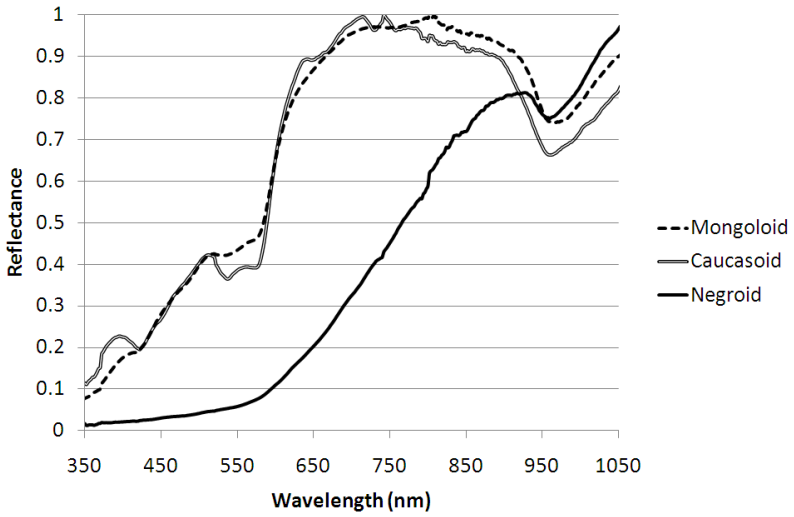

Fig. 4.1 An image of light reflection as a function of skin colour [36]

4.3 Design Specification

For the purpose of developing this system as a tool for test engineers here at Philips as well as a final product for the consumer, its essential for the design to meet a set of specification. These specifications will set the reference standards for any future improvements and modifications. These requirements are discussed in details in the following sections.

4.3.1 Field of View

The system should be capable of measuring skin doming at each individual slot. Since the average width between 2 slots is 0.25mm and for holes is 1.5mm, hence the receiver should have a comparable field of view of the order of 0.25mm-0.5mm. As no surface mounted device (SMD) IR emitters and IR photodiodes of size 1.6mm×0.8mm (0603 package) or 1.0mm×0.5 mm (0402 package) were commercially available with very low directivity (i.e 10 degree or less), hence it was concluded that an alternate solution needs to be devised. This gave birth to the idea of using FOC as a light guide for both emitter and receiver. Fine cut FOC of about 5.5mm length and 0.5mm

diameter were polished using very fine grain sand paper and then again polished using Ethanol. Figure 4.2 shows the surface finish of polished FOC.

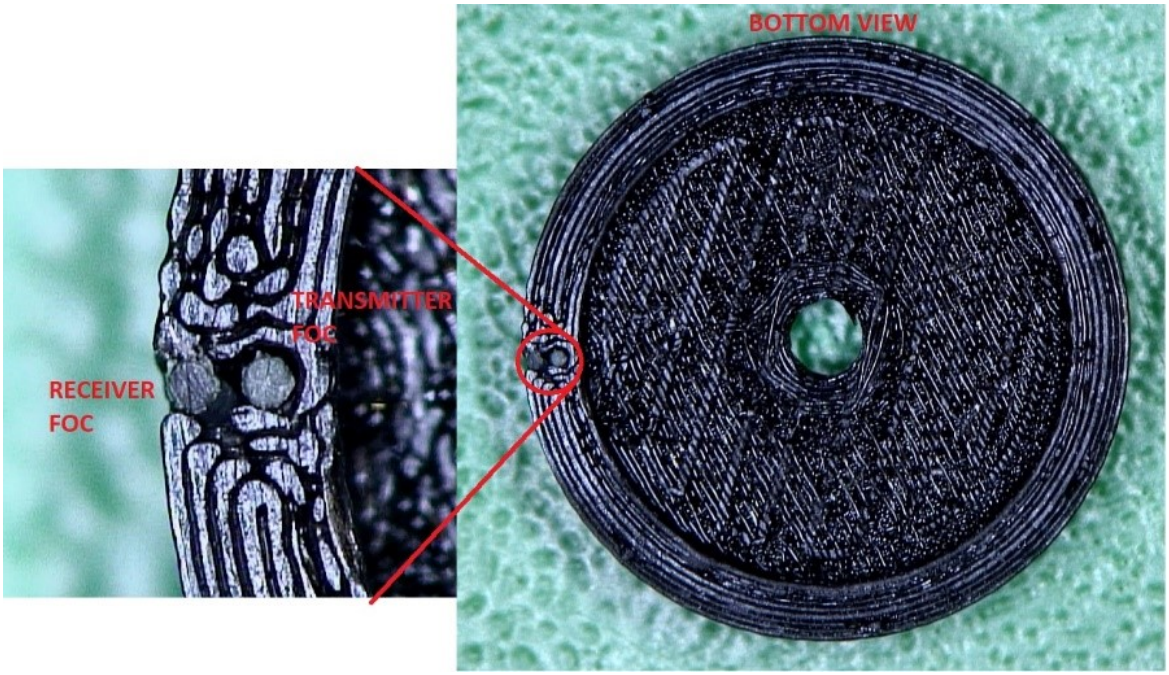

Fig. 4.2 Surface finish of polished FOC

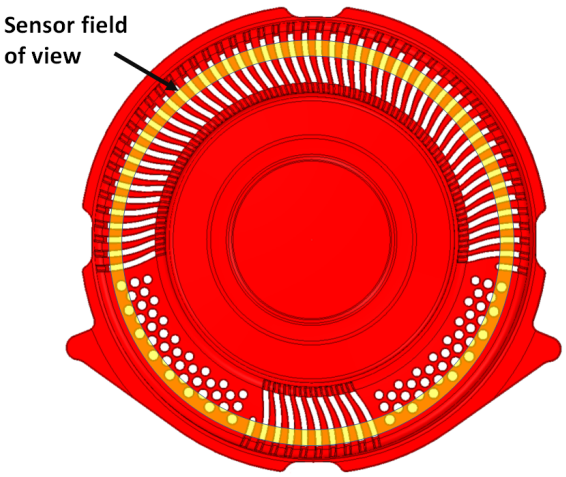

Fig. 4.3 Image representing the field of view (yellow circle) of the sensor, it shows approximately how many slots and holes it actually see.

Fig. 4.3 shows the approximate field of view of the sensor. Due to the narrow field of view the sensor doesn't see all holes/slots. Although there are a total of 76 holes

and 58 slot(+2 minislots) in the cap but due to narrow field of view and alignment of the sensor FOC it sees only 58 slots and 16 holes, or a total of 74 slots and holes.

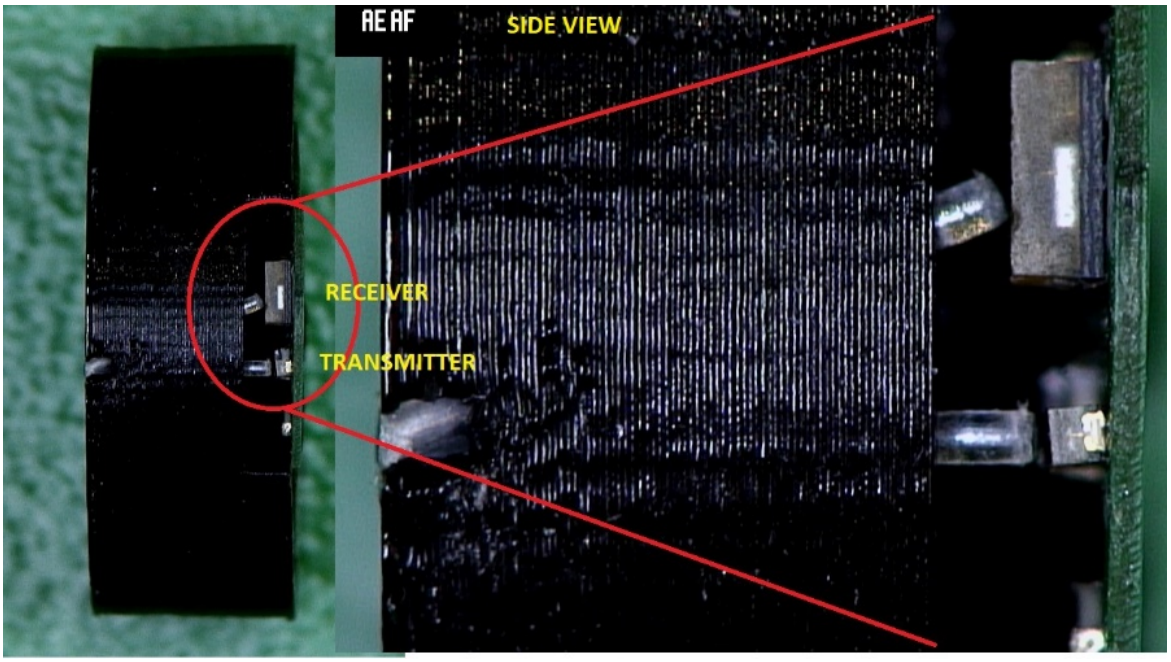

Fig. 4.4 3D printed part with tunnels for the FOC that align perfectly with the IR emitter and receiver active chip area

A 3D printed part was designed with tunnels for the FOC to fit precisely over the IR emitter and receiver, which is visible in figure 4.4.

4.3.2 Optical Crosstalk and Optical Coupling

Optical cross talk was reduced and optical coupling efficiency increased by seperating the emitter receiver pair by 3D printing rooms around them, refer fig. 4.5. Also in second generation of PCB design of the optical measuring platform in chapter 5 IR emitter receiver pairs with narrower directivity are used. Narrow directivity makes sure that all light is directed into the FOC and not dispersed in the surroundings causing optical crosstalk. The light is incident on the metal cap through the FOC and since most surfaces behave like a Lambertian surface, the metal cap too disperses the incident light equally in all directions [10]. This would have caused the receiver without an FOC light guide to pick up all these ambient reflections and produce a fixed DC offset in the sensor output.

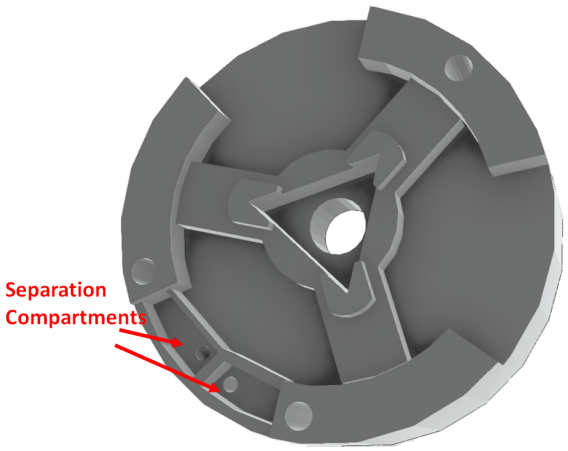

Fig. 4.5 CAD image of 3D printed part with seperation rooms for emitter and receiver to prevent optical crosstalk

4.3.3 Sampling Time

The response time of the IR emitter is 12ns and the response time of IR receiver is 100ns. Since the response time of the emitter time is negligible in comparison to the shaving cutter rotation we will not be considering the response time of the IR emitter receiver pair. The shaving cutter is rotating at 2100(±200) RPM and as stated in 4.3.1 the sensor sees a total of 74 slots/holes.

Table 4.1 Response time calculation with worst case RPMs for cutter

Calculations	Cutter RPM		
	Max	Nominal	Min
RPM	2300	2100	1900
RPS	2300/60 = 38.33	2100/60 = 35	1900/60 = 31.67
Time per round	26.0ms	28.6ms	31.5ms
Time per slot/hole	26ms/74 = 351μs	28.6ms/74 = 386μs	31.5ms/74 = 426μs
Sampling time (x5)	351μs/5 = 70μs	386μs/5 = 77μs	426μs/5 = 85μs
Sampling rate	14.3kSPS	13.3kSPS	11.76kSPS

If the ADC sampling and IR emitter switching is perfectly synchronised with the slots passing above the sensor then a sampling time of 351μs to 426μs depending on the RPM are ideal, as it measures at the exact correct instant. But, since the RPM is not constant and the ADC sampling and IR emitter switching is not synchronised

with the slots passing above the sensor hence a high sampling rate is needed. Thus, as per calculations in table 4.1 to generate high fidelity signal of the reflections, our system samples at about 14.3kHz which is 5 times the highest rate. Fig. 4.6 shows the difference in 1x sampling rates vs 5x sampling rate.

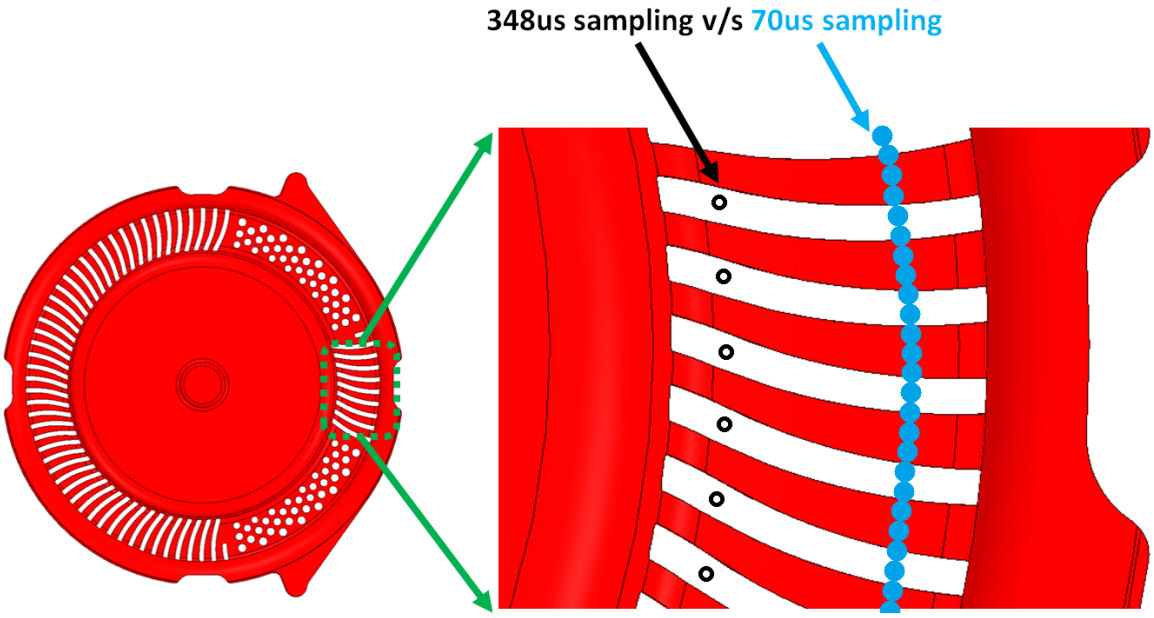

Fig. 4.6 Sampling instant for perfectly synchronised(1x) sampling (in black) versus unsynchronised high speed(5x) sampling (in blue).

4.3.4 Power Consumption

The initial proof of concept prototype of energy harvester has demonstrated the ability to generate about 3mW of power [18]. It is speculated based on theoritical calculations that an improved prototype of the initial proof of concept can generate about 25mW of power. But the requirements for the energy harvester power output was 50mW [18]. Hence the maximum power budget of the whole system should be approximately 45mW. A detailed analysis of power consumption of the design proposed in this thesis is done in chapter 7.

4.4 Calibration

Calibration of the sensor system is critical in achieving an accuracy of 10μm and is equally complicated. Presently, an OCT machine is used to measure the skin doming

through the shaving cap slots and holes. The cap is placed under the machine to view the skin doming through the stationary metal shaving cap. Performing skin doming to calibrate the sensor while the cutter is in operation under the OCT machine is not feasible. Thus, a new calibration approach and mechanical assembly for calibration is required. Hence a new approach has been taken. In this approach the cap would be rigidly fitted on a fixed support. The artificial skin is places in between this rigid fixed support (on which the shaving cap is fitted) and an L shaped precise micrometre positioning horizontal translation table with a resolution of 20μm. The image of the setup is shown in fig. 4.7.

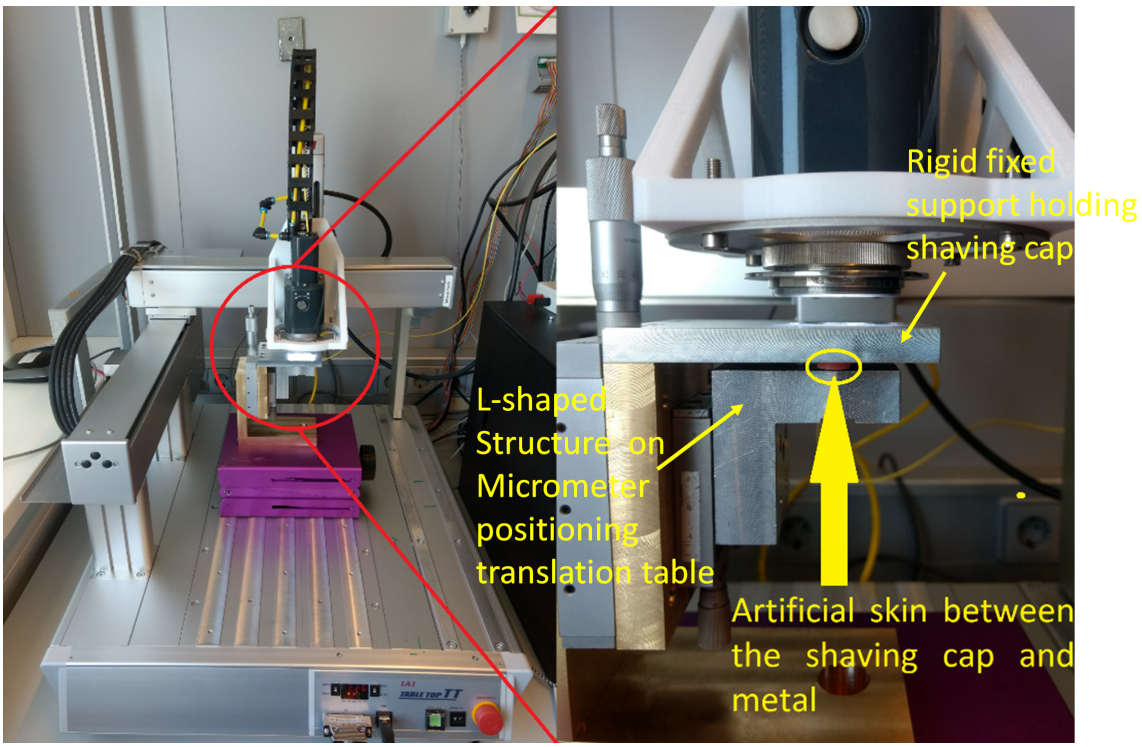

Fig. 4.7 View of the setup under optical coherent tomography machine

Figure 4.7 shows the setup under the OCT machine. In this setup the L shaped precise micrometre positioning translation table is moved in steps of 100μm to push the artificial skin against the rigidly fixed shaving cap and measure the skin doming.

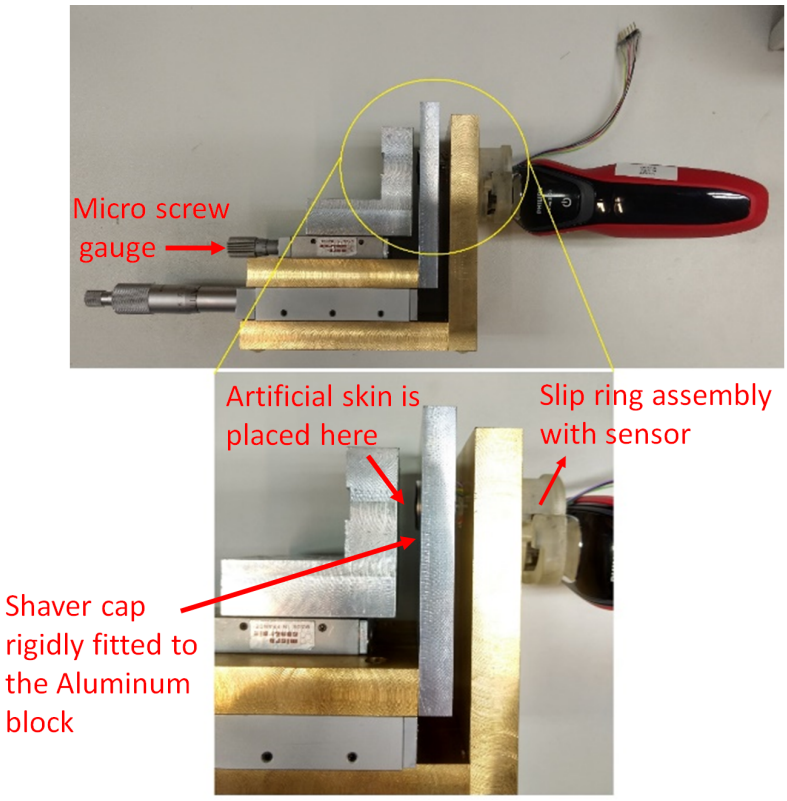

Fig. 4.8 Close-up view of the newly designed calibration set-up with micrometre screw gauge

The skin doming through the metal slots can be seen in figure 4.9 and 4.10. The readings of micro screw gauge of the translation table are noted corresponding to skin doming in μm as measured using OCT machine. This same reading of the screw gauge of the translation table will be set again to push the skin against the metal cap but this time the sensor system will be rotating inside the shaving cap. The intensity of reflection will be directly related to the amount of skin doming in μm as measured under the OCT machine for that reading of micrometer screw gauge. The results of these readings/calibration are discussed in chapter 7 of this thesis.

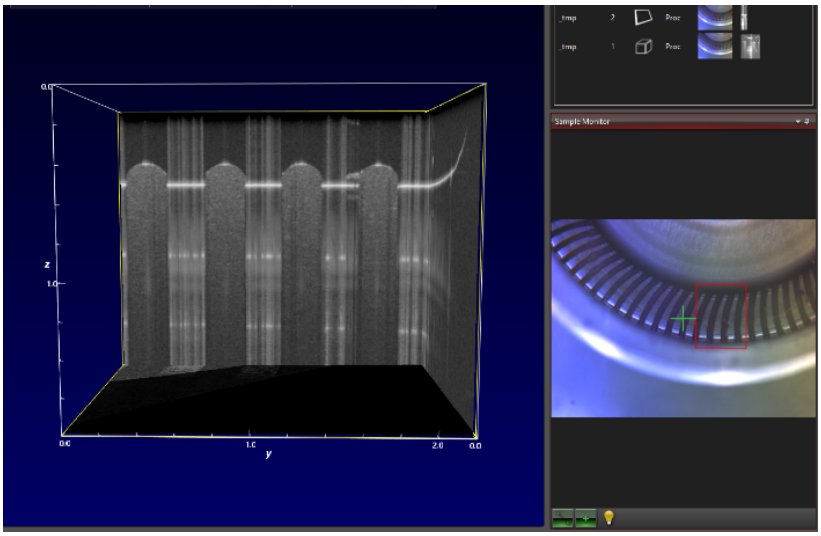

Fig. 4.9 OCT image of the metal cap with +100μm skin doming

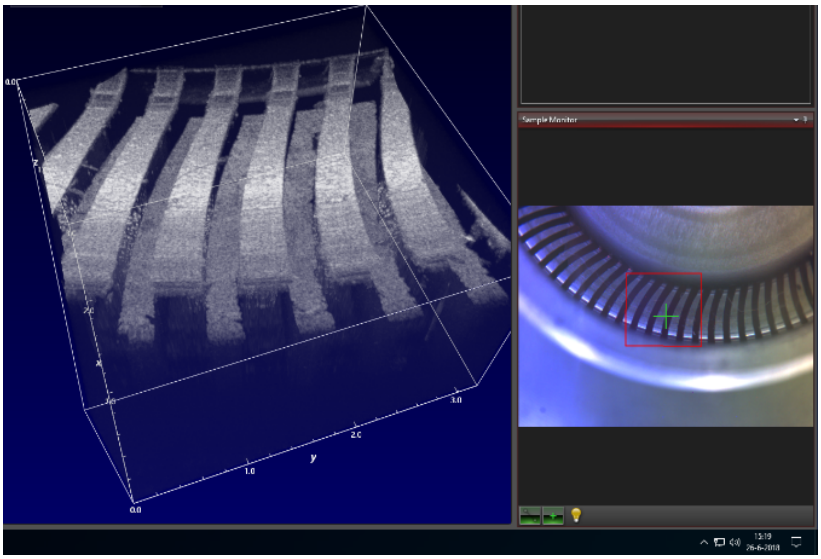

Fig. 4.10 OCT image of the metal cap with -100μm skin doming

4.5 Slip Ring Assembly

Fig. 4.8 shows the micro screw gauge setup used in fig. 4.7. This setup is also used to measure skin doming with the sensor electronics along with the actual shaver. The additional component other than the shaver unit is the slip ring assembly. The slip ring assembly connects the signals from the rotating sensor assembly in the cutter

to the outside world. This is a critical component since its needed to transmit the processed data to the outside world while the sensor system is measuring while rotating at 2100 RPM. An exploded view of the slip ring assembly is shown in fig. 4.11.

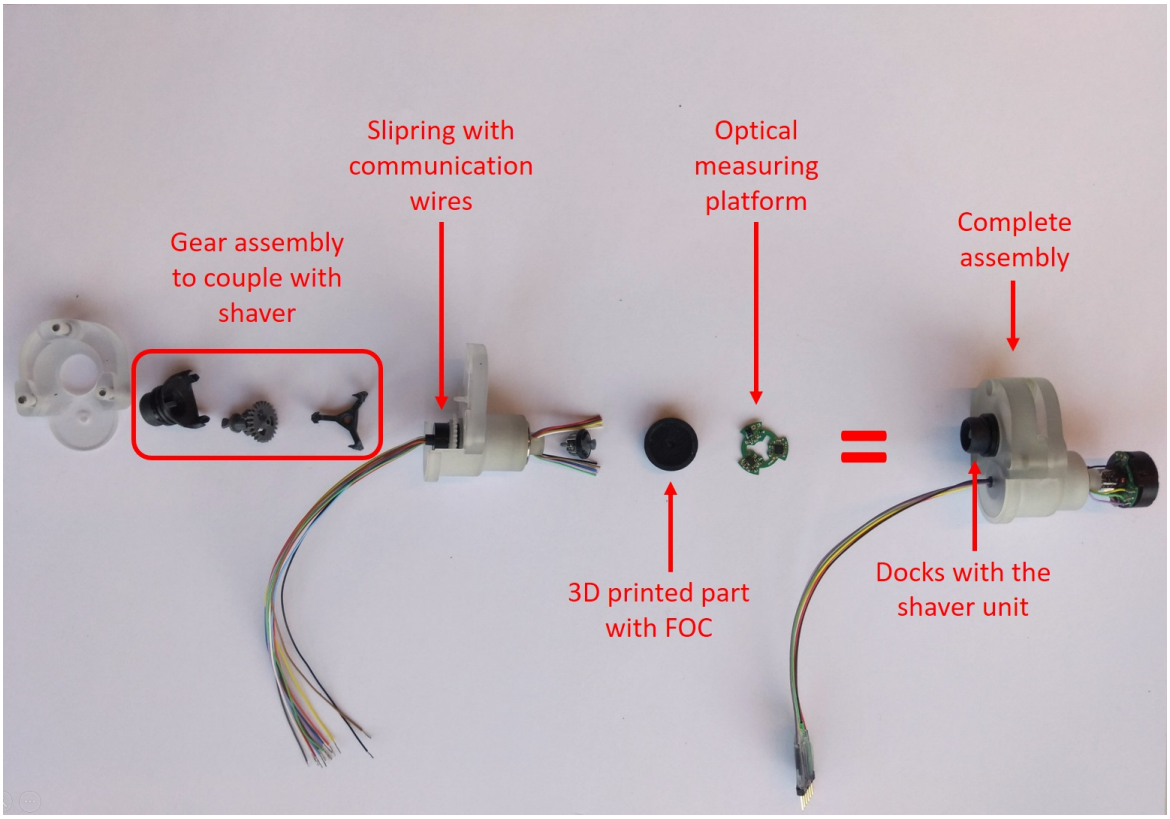

Fig. 4.11 Slip ring assembly

Chapter 5

Optical Measuring Platform

This chapter includes details about the circuit design of the measuring system that contains the sensor, its signal conditioning circuit and signal processing circuit. This printed circuit board (PCB) which is on the cutter is collectively defined as the Optical Measuring Platform (OMP). The OMP includes all parts within the blue dash line in figure 3.1 except the blocks with the orange dots which are reserved for future development/implementation. The following sections discuss the circuit design and requirements for the first and second generation of the design.

5.1 Circuit Design for First Generation PCB

As discussed previously that there are major space constrains for the PCB, and the circuit has to have minimalistic electronics to do the task while meeting all the design requirements. The total area of the developed PCB is $1.82cm^2$. This area only accounts the top surface area of the PCB and not the bottom since placement of parts on the bottom layer of the PCB is not possible due to the presence of contoured metal surface of the cutter.

Due to the area constrains, one of the requirements of this thesis is minimalistic circuit design so that all electronics fit into the PCB. This section will be subdivided into the subsections dedicated for the microcontroller, sensor , signal conditioning circuit and power regulation.

Figure 5.1 and 5.2 show the top and bottom view of the first version of the OMP PCB. Figure 5.3 shows how the PCB will be placed in the cutter. Design improvements for version 1 were made in version 2 of the OMP.

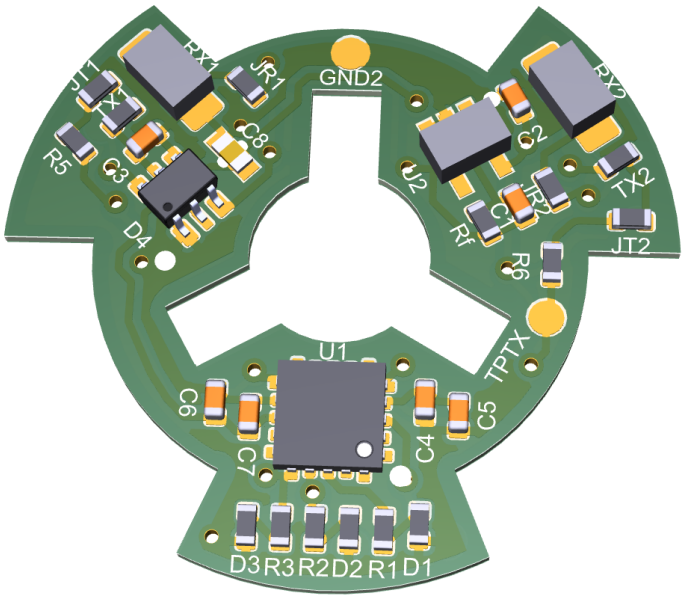

Fig. 5.1 Top 3D view of version 1 PCB of OMP

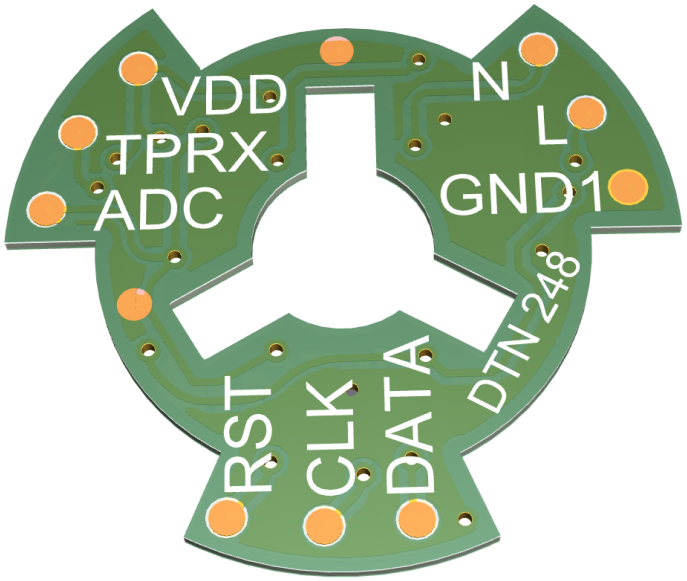

Fig. 5.2 Bottom 3D view of version 1 PCB of OMP

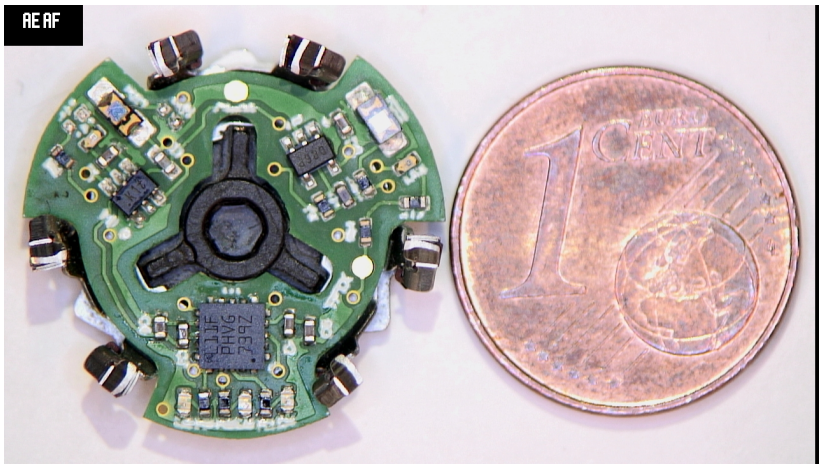

Fig. 5.3 Top view of version 1 PCB (of diameter of approx 1.94cm) mounted on the cutter next to a 1 cent Euro coin for size estimation.

5.1.1 Microcontroller

There are four main design requirement for choosing a microcontroller.

- **Footprint:** The footprint of the microcontroller should be less than or equal to 3mmx3mm and vertical height not more than 1mm.
- **Ultra low power:** The micro controller should be a at least 16bit ultra low power series which is capable of functioning until at least 1.8V with low power peripheral support such as timers, communication and ADC.
- **Communication**: It should support UART, SPI, I2C communications for data transfer for GUI integration, post processing of data and for later integration to a wireless transmitter.
- **Built-in clock sources:** Due to space constraints built-in clock sources upto at least 16Mhz are required.

With these given design parameters for the microcontroller after comparison and survey of microcontrollers from Texas Instruments, NXP, Renesas, Microchip and ST Microelectronics. ST Microelectronics STM32L011x series microcontroller was chosen as it met with will all the above requirements with good compilers and community support.

The PCB designed with STM32L series microcontroller has supporting circuitry for in-circuit programming and in-circuit debugger.

5.1.2 Emitter Receiver Pair

The performance and size criteria for the emitter receiver pair are as below:

- **Sensor Wavelength**:Based on the outcomes of section 4.2 an IR Emitter Receiver pair tuned at 940nm wavelength is required.
- **Footprint:** The footprint of sensor is one of the most important criteria after the wavelength. Since the sensor is placed on the edge of the PCB[1], the footprint should be no greater than 2.0mm×1.25mm (0805 package) and height at most 1mm.
- **Directivity:** The directivity of the emitter receiver pair is another critical parameter for selection of the IR emitter and receiver. It is critical because a high directivity will result in majority of IR emission going into the FOC with much better optical coupling. This in turn enables the emitter to be fired at much lower power to have the same level of sensitivity at the receiver.

  The required directivity for the design is calculated as follows:

For an ideal IR emitter the emitted IR radiation is perfectly rectilinear (i.e with ±0 degree directivity). This would result in some surface (α) of FOC will not receiving emitted IR radiation as shown in fig. 5.4, if the emitters active chip cross-section is less than the FOC diameter.

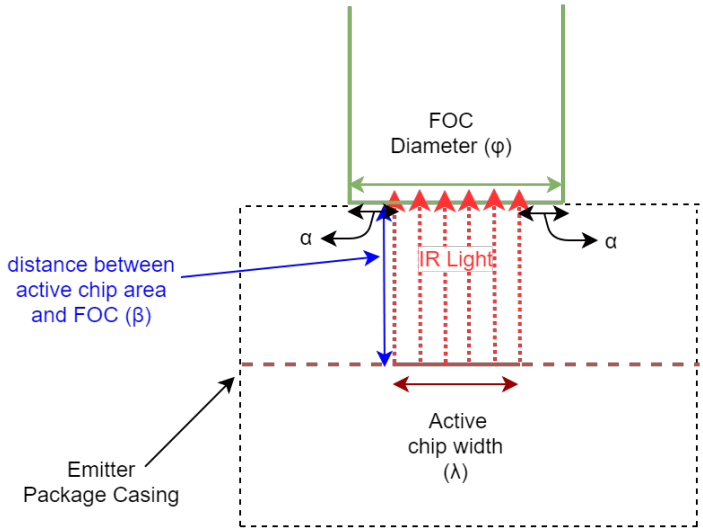

Fig. 5.4 Side view of ideal emitter with nil directivity

[1]Refer RX1-TX1 and RX2-TX2 in fig. 5.1 to have an understanding of area available for the emitter receiver pair

Thus, for a given emitter with active chip area less than the FOC cross-sectional area, some directivity angle is required. This is shown in fig. 5.5 for our setup and is calculated below:

Cross-sectional length not receiving IR emission on each side of FOC

$$\alpha \Rightarrow \quad \frac{(\phi - \lambda)}{2}$$

Thus, the required directivity as per fig. 5.5 is twice the value of (θ) :

$$Tan(\theta) = \frac{\phi - \lambda}{2\beta} \;\Rightarrow\; \theta = \tan^{-1}(\frac{\phi - \lambda}{2\beta}) \tag{5.1}$$

The below mentioned emitter receiver pairs were chosen which fulfilled the criteria of wavelength of 940nm, as well as footprint/size requirements, but not the directivity. IR emitter receiver pairs within the given footprint/size constraints were not available with directivity less than ±60 degrees. Hence TEMD7100X01 [16] as IR PIN Photodiode (receiver) and SFH4043 [17] as IR emitter were the best available options. This drawback was taken as an opportunity to verify the hypothesis that if indeed high directivity is needed to see each single slot/hole of the shaver cap. Also to identify the best physical placement the emitter receiver pair, the emitter receiver pairs are placed on the PCB design in 2 orientation. Please refer RX1-TX1 and RX2-Tx2 in fig. 5.1 for different placements and orientation of the 2 emitter-receiver pairs .

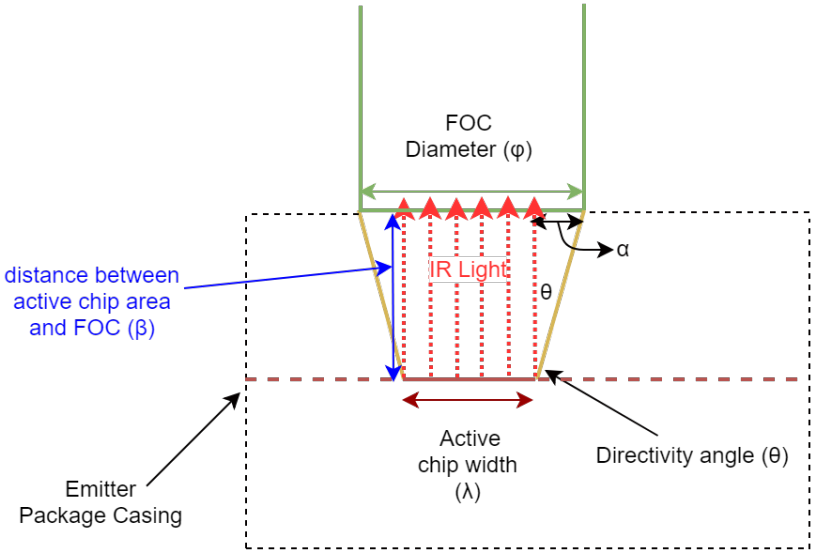

Fig. 5.5 Side view of emitter with required directivity

The equivalent photodiode model for TEMD7100X01 is given below, this photodiode model is used for calculations in the following sections:

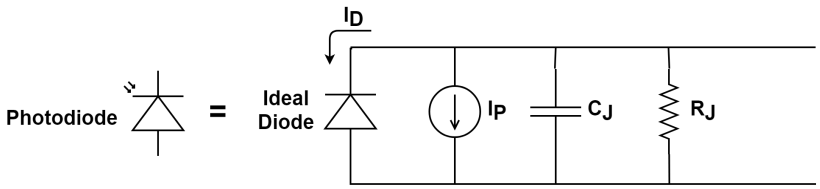

Fig. 5.6 The equivalent circuit for a photodiode

where in fig.5.6:

$I_P = Currentsource(photocurrentgeneratedbytheincidentlight)$
$R_J = Junctionshuntresistance$
$C_J = Junctioncapacitance$
$I_D = Darkcurrent$

For the chosen photodiode TEMD7100X01 [16] the values are as follows:

$I_P = 3\mu$A (photocurrent generated by peak light intensity)
$R_J = 10G\Omega$
$C_J = 4pF$
$I_D = 1nA$

5.1.3 Signal Conditioning Circuit

The signal processing of the raw photodiode output is critical. This section discusses design equations, circuit component selection and optimizations that are implemented in this design and in the next iteration of the design. A photodiode responds to the change in received light intensity by generating photo-current. This photo current is of the order of a few μA depending on the type of photodiode and active chip area. The peak photo current for the selected photodiode TEMD7100X01 is 3μA [16]. Hence this few μA photo-current needs to be converted to a stronger signal level either by conversion to voltage or frequency etc. Based on the selected emitter receiver pairs there are six main design requirement for the signal conditioning circuit:

- **Current to Voltage Conversion:** The signal conditioning circuit should be able to convert the photodiodes photo current to voltage.
- **Amplification:** The signal conditioning circuit should provide a peak voltage of 3.3 volts at maximum response of the photodiode.

- **Bandwidth:** The bandwidth of the signal conditioning circuit should be greater then 8kHz.
- **Power Supply:** It should operate with single supply power from atleast 2.4V to 3.3V.
- **Offset:** The signal conditioning system should not induce offset in the conditioned output signal or in case of using Opamps the input bias current should be of the order of few pico amperes.
- **Footprint and component count**: Due to PCB area constrains the total area cost should not be more than $54mm^2$.

The output signal of the photodiode can be either interpreted as a voltage or current. The most obvious approach used for signal conditioning circuit while using photodiodes is using a transimpedance amplifier (there after referred as opamp). For such applications a current monitoring is preferred as it offers much improved linearity, offset and bandwidth performance. But since the microcontroller chosen in section 5.1.1 accommodates only voltage signals at its GPIOs hence the design approach is based on a simple minimalistic current to voltage converter using an opamp and feedback resister.

Operational Amplifier Mode of Operation

Based on the above mentioned design constrains for signal conditioning circuit, a survey was done for opamps especially designed for transimpedance amplifications. Based on the survey of competing options Microchips MCP6491 opamps were finalised as the opamp that meet or exceeded the design requirements.

The opamp for such an application like transimpedance amplification can be configured into two modes, i.e photoconductive mode and photovoltic mode. Both the configuration have their own applications. In photo conductive mode the photodiode has a reverse bias voltage across it, this reduces the diode junction capacitance and facilitates high speed operation. The photo conductive mode performs best when the photodiode is detecting light switching at high speed i.e in excess of 350kHz or more. On the contrary the the photovoltic mode offers higher sensitivity and works well with ultra low level light applications along wilt better immunity to temperature variations [37]. Since this mode has zero voltage potential across the photo diode hence no dark current flows throught the photodiode and linearity and sensitivity are maximised [38]. Hence for our applications photovoltaic mode of operation is best suited . A typical

application circuit of "photovoltaic mode" of operation is given below.

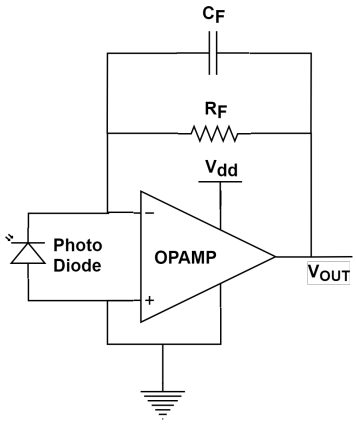

Fig. 5.7 Typical application circuit of "photovoltaic mode" photo diode amplifier

In this mode the output of the circuit is defined by: $V_{OUT} = I_P \cdot R_F$

5.1.4 Design Calculations

Based on the photodiode specifications in section 5.1.2, following values are calculated based in the model in figure 5.6.

Feedback Resistor

The starting point of the design calcualtion is the V_{OUT} value which is to be set to V_{dd} which in our design is 3.3V. Since the photodiode has a very small photocurrent due to use of FOC, the photodiode in the design with the FOC assembly is able to generate only about 1.6μA of peak photo current. Hence R_F is set to be a large value to swing the opamps output voltage to V_{dd}. In practicality there is some input offset voltage V_{OS} which needs to be accounted for while doing the calculations. The input offset voltage for MCP6491 opamp is 1.5mv hence

$$V_{OUT} - V_{OS} = I_P \cdot R_F \;\Rightarrow\; V_{OUT} = I_P \cdot R_F + V_{OS} \tag{5.2}$$

$$3.3 - 0.015 = 1.6\mu A \cdot R_F \Rightarrow R_F \approx 2M\Omega$$

Thus, a 2MΩ resistor with tight tolerance(1%) is used.

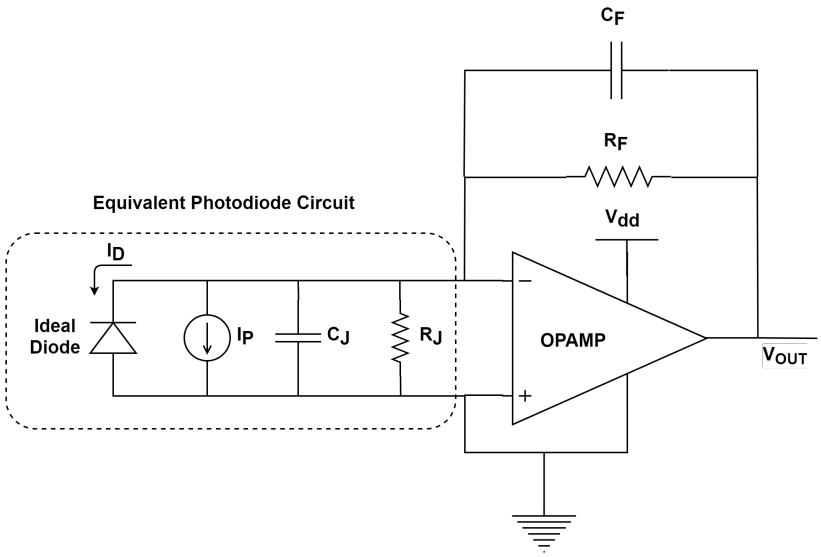

Fig. 5.8 Photodiode amplifier in photovoltic mode of operation using feedback capacitor.

Feedback Capacitor

At the maximum permitted speed of the cutter i.e 2300 RPM or 38.3 RPS, the highest frequency received by the receiver from the reflection of the passing slots is $\approx$ 2.9kHz. Thus the required bandwidth of the signal conditioning circuit can be set to $\approx$ 4kHz. For these values of frequency and resistor, the feedback capacitor value is calculated to be 20pF, hence the nearest standard value of 22pF is selected. The calculations are as follows:

$$C_F = \frac{1}{\left(2\pi \cdot R_F \cdot f_c\right)} \Rightarrow \frac{1}{\left(2\pi \cdot 2M\Omega \cdot 4kHz\right)} \approx 20pF$$

Opamp Gain Bandwidth

Different factors limit the designs bandwidth, usually this results primarily from the photodiodes junction capacitance (C_J) , differential input capacitance of the opamp (C_{DM}), the common mode input capacitance of the inverting input (C_{CM}) and parasitic capacitances(C_S) . Hence the calculation of the gain bandwidth for the opamp takes into account these capacitances and needs to be investigated. The total capacitance of the design is

$$C_{tot} = C_J + C_{DM} + C_{CM} + C_F + C_S$$

Thus, the required opamp GBW for circuit stability is:

$$GBW > \frac{C_{tot}}{2\pi \cdot R_F \cdot C_F^2} \Rightarrow GBW > \frac{\left(C_J + C_{DM} + C_{CM} + C_S + C_F\right)}{2\pi \cdot R_F \cdot C_F^2} \tag{5.3}$$

Putting all values in 5.3 and neglecting C_S as its negligible for the size of the PCB and $C_{DM} + C_{CM} = 12\text{pF}$ [38]:

$$GBW > \frac{\left(4pF + 12pF + 22pF\right)}{2\pi \cdot 2M\Omega \cdot 22pF^2} \approx 6.247kHz \tag{5.4}$$

Hence the system needs to have a GBW $> \approx 6.247$ kHz which is well within the specifications of MCP6491 opamp.

5.1.5 Rectification Circuit

Only a brief overview of the power regulation unit will be discussed since the passive rectification of the energy harvester signal is now replaced by a new research done at Philips Drachten. This new research uses microcontroller's general perpose input/output (GPIO) pins for active rectification [19].

In the first generation design the rectification of the AC generated by the energy harvester is done using BAV99S, which is a high speed switching diode configuration which is connected as a full wave rectifier. In theory, any capacitance affects the performance of high speed or high frequency circuits. The RC time constant represent the delay in the time domain and pole location in the frequency domain. Thus in order to rectify high frequency AC signal of the order of tens of kHz we need to minimise capacitance. The main reason for choosing BAV99S was its low junction capacitance and very small footprint [39]. But since this conventional passive rectification approach is replaced by the new active rectification approach developed at Philips which used microcontrollers GPIOs for active rectification [19], this rectification circuit is removed in the next PCB design for OMP. The final schematics of PCB version 1 is as shown in fig.5.15.

5.2 Circuit Design for Second Generation PCB

Although keeping the design constrains in mind first generation of PCB for OMP met all design criteria and gave good results , but had some minor inefficiencies and

deficiencies . The only inefficiencies was that both the IR emitter/receiver had very wide directivity(±70 deg) , making the optical coupling of the IR radiation into the FOC very poor and ineffecient as majority of the IR light goes into the environment and not FOC refer fig 5.9 .

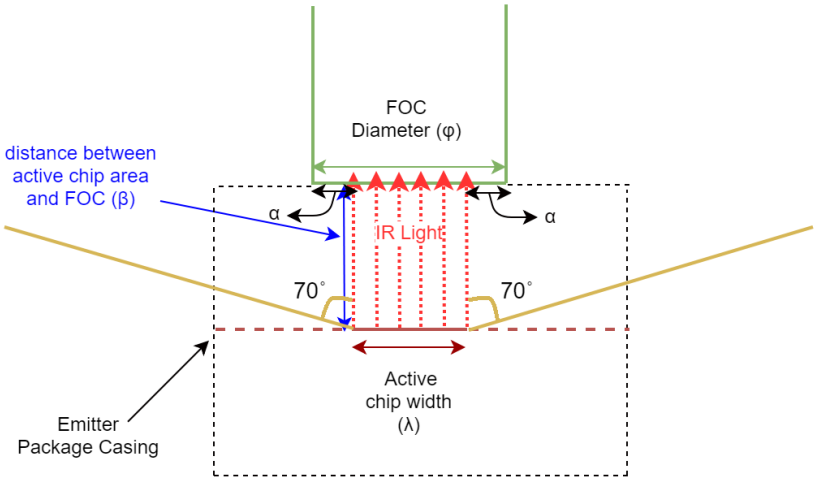

Fig. 5.9 Wide directivity of IR emitter/ receiver as the major reason for optical coupling losses in first generation of OMP design.

The following sections will look into improving the short falls of the previous design, such as optical coupling losses, reduce the over all power consumption of the system and further improve the photodiode amplifier performance response.

5.2.1 Design Improvements

The new PCB design for the second generation was made more modular inorder to test multiple configurations on the same PCB. The size and the form factor of the second generation PCB is exactly the same as the first generation . There are the following major improvements/changes over the first generation of the design.

Narrower Directivity of the Emitter-Receiver pair

The IR emitter operation contributes to about 87 % of the total power consumption of the whole system. This is because of reason stated in the above section. This drove the design aim to calculate the ideal required directivity of the emitter and receiver for the given FOC. The narrower the directivity (θ) , the better the optical coupling and lower the power required to have the same sensitivity at the photodiode. Hence, based on equation (5.1) the ideal required directivity is calculated below:

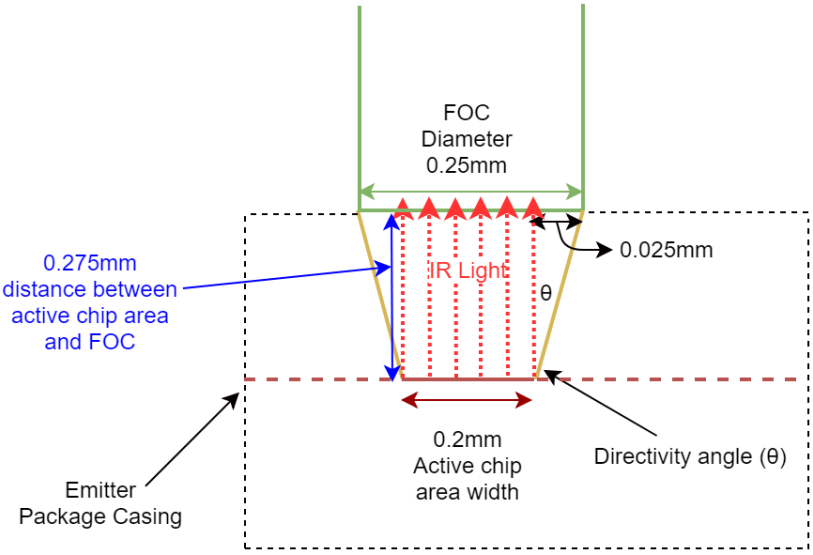

Fig. 5.10 Side view of emitter with required directivity

Diameter of the FOC = 0.25mm.
Width of the active chip area[2] = 0.2mm.
Approx. depth of active area from the surface of SMD package [3] [17] = 0.275mm.

$$0.25mm - 0.2mm \;\Rightarrow\; 0.05mm \text{ or } \frac{0.05}{0.2} \;\Rightarrow\; 0.025mm \text{ on each side of FOC.}$$

Thus the requirement for our design as per (5.1) is :

$$Tan(\theta) = \frac{0.025}{0.275} \;\Rightarrow\; \theta = \tan^{-1}\frac{0.025}{0.275} \;\Rightarrow\; \theta \approx 5.2 \;\; Deg$$

Or, the required directivity is twice the value of (θ):

$$2\theta = 10.4 \;\; Deg$$

Based on the above calculation IR receiver (TEMD1020) and emitter (SFH4045N) with very narrow directivity of ±15 deg and ±9deg respectively were chosen as these were the closest possible value of directivity commercially available in SMD with 940nm wavelength [40],[41].

[2]For majority of commercially available 940nm IR emitters with 0402 package
[3]For majority of commercially available 940nm IR emitters with 0402 package

Reduced Optical Crosstalk and Improved Modularity

The design modularity was another improvement done in the second generation. This would help to rapidly test the effect on performance of the design due to different circuit configurations on the same PCB.

(a) Optical Crosstalk

One of the major design hindrance both in terms of electronic and mechanical design was the issue of optical cross talk. Due to the extreme space constrains on the PCB the IR emitter and receiver had to be placed close to each other on the PCB. This caused alot of optical crosstalk especially when IR emitter is fired at high power. This required mechanical modifications in the design casing of the 3D printed part which provided a mechanical barrier and prevented optical crosstalk to a great extent. Hence in this second generation the PCB itself is used as a mechanical barrier against optical crosstalk and simplify the mechanical design. This has been achieved by using a reverse mounting IR Emitter with very narrow directivity of ±9deg. The reverse mounting provides a natural mechanical barrier against optical cross talk with the receiver by using the PCB material as the shield. More over in order to use IR emitter with narrow directivity a lens dome SMD IR emitter was required. Due to the height constrains this IR emitter with lens dome could not have been top mounted. Hence reverse mounting was the best solution. Refer fig. 5.11 and 5.12 for the hole and reverse mounting pads on the bottom view of the PCB marked as TX2.

(b) Modularity

The design was made keeping modularity in mind, thus two placement orientations of emitter was made, refer TX1 in fig.5.11 and reverse mounted TX2 in fig.5.12 respectively for placement orientations. Only one of them would be populated on one board , thus we can analyse which orientation is better using only one PCB design. Other than this compensation of errors due to using very large gains and input bias current of the pins is also incorporated in this design which can be selected by means of jumpers.

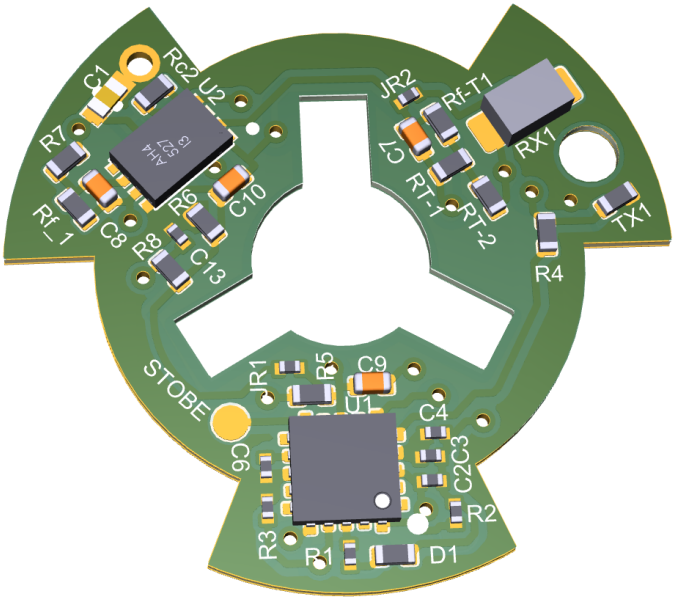

Fig. 5.11 Top 3D view of version 2 PCB of OMP

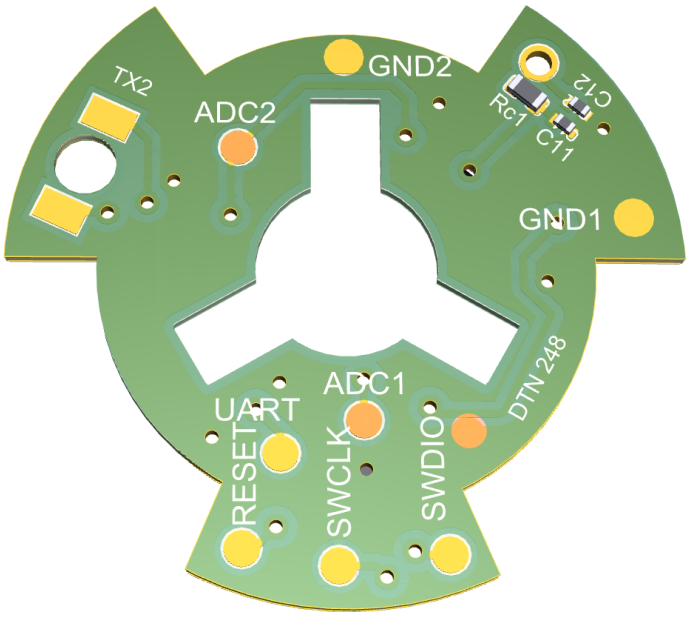

Fig. 5.12 Bottom 3D view of versi on 2 PCB of OMP

Figure 5.11 and 5.12 show the top and bottom view of the second version of the OMP PCB.

Compensation for Input Offset Error

Although the input bias current is very small for MCP6491 at 350pA (maximum) [38] but a large feedback resistance for large amplification can result in higher error due to this input bias current. Since with the new IR emitter will be operated at much lower forward current than 27mA , the photo current at the photodiode will also be much weaker. To counter this the opamp will need a much higher feedback resister to have an output of 3.3V for maximum photo current. This high feedback resistance along with the input bias current would result in an error in the output of the opamp. Hence, this is countered by means of compensation resistor at the non inverting terminal or by means of a T-network for the feedback resistor or combination of both. In fig. 5.13 I_D is the total diode current which is a sum of the photocurrent (I_P) and leakage current (I_L).

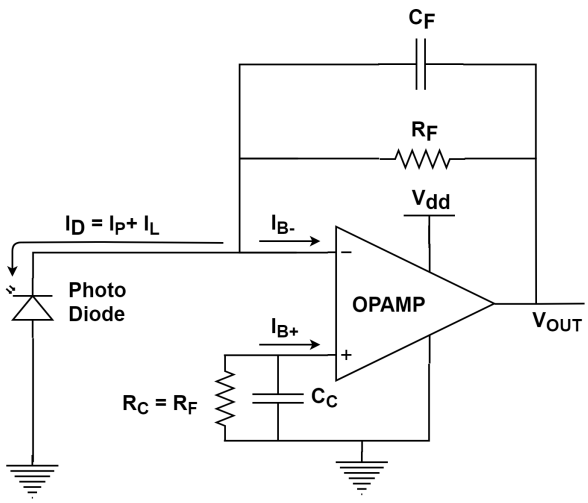

Fig. 5.13 Input offset current as cause of output signal error

Although the error due to the opamp input offset current is compensated in a simpler way by using a compensation resistance (R_C) at the non inverting terminal. But this (R_C) produces a counter acting compensation voltage equal to -$I_{B+} \cdot R_C$. However in our application this (R_C) develops a voltage across the photodiode and encourages enhanced photodiode leakage current (I_L) . Thus, this leakage current adds additional offset voltage. The combined output offset voltage (V_{OS}) is given by

$$V_{OS} = \left(I_{B-} \cdot R_F + I_L \cdot R_F - I_{B+} \cdot R_C\right)$$

on perfect resistor matching of R_C and R_F

$$V_{OS} = \left(I_{B+} - I_{B-} + I_L\right) \cdot R_F \tag{5.5}$$

As evident from 5.5 a large R_F will result in a large V_{OS}. Hence to minimize this second generation design also implements a Tee-network to counter this.

Tee-Network

The new design need not use a very large single value feedback resister due to reasons state in the above section but instead uses a Tee-network as shown in fig. 5.14.

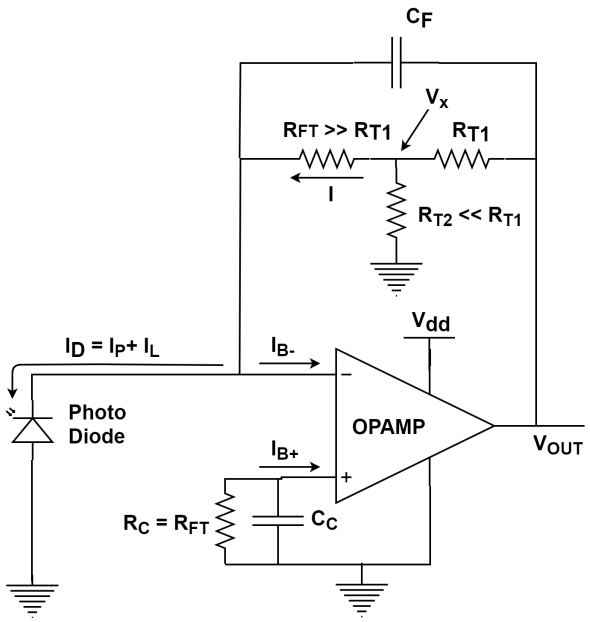

Fig. 5.14 Error compensation using a Tee network

Fig. 5.14 shows the R_F equivalent Tee-network but using much smaller resistance values than used in fig. 5.13. The equivalent value R_{Feq} of the Tee-network is calculated as follows:

Let the voltage at the junction of R_{FT}, R_{T1} *and* R_{T2} *be* V_x then

$$V_x = V_{OUT} \cdot \left(\frac{R_{T2}}{R_{T1} + R_{T2}}\right)$$

The current (I) flowing through R_{FT} is V_x / R_{FT} combining the two yields

$$I = \frac{V_{OUT}}{R_{FT}\left(1 + \frac{R_{T1}}{R_{T2}}\right)} \text{ or}$$

$$R_{Feq} = R_{FT} \cdot \left(1 + \frac{R_{T1}}{R_{T2}}\right) \tag{5.6}$$

From 5.6 we see that the value of R_{FT} is reduced by a factor of $\frac{1+R_{T1}}{R_{T2}}$, hence the offset voltage from 5.5 is reduced by the same factor for the Tee-network.

Thus for the second generation design the values of the Tee-network for the same opamp output of 3.3V at peak photocurrent are as follows:

Using equation 5.6 for $R_F = R_{Feq} = 2\text{M}\Omega$, the values of R_{FT} for Tee-network for standard 1% resistor values of 23.7kΩ and 11kΩ for R_{T1} *and* R_{T2} respectively is:

$$2M\Omega = R_{FT} \cdot \left(1 + \frac{23.7k}{11k}\right) \;\Rightarrow\; R_{FT} = \frac{2M\Omega}{\left(1 + \frac{23.7k}{11k}\right)} \approx 634k\Omega.$$

For this R_{Feq} of 2MΩ using the Tee-network the calculated V_{OUT} is a sum of 5.2 and 5.5 is:

$$V_{OUT} = I_P \cdot R_{Feq} + \left(I_{B+} - I_{B-} + I_L\right) \cdot R_{FT} \tag{5.7}$$

Thus from 5.7 its evident that the error due to feedback resistance in first generation of the design has reduced by a factor of more than 3 times due to the reduced value of R_{FT} yet yielding the same gain.

Improved Bandwidth by Two Stage Amplification

The opamp MCP6491 used in the first generation of the design was a single opamp package, hence the design did all amplification on single stage. Where as this design has TDFN-8 2mmx3mm dual opamp package MCP6492. Hence the total amplification of the photodiode signal will be done in two stages which will improve the bandwidth of the design. This increased bandwidth will enable the circuit to further amplify the signal and save more power by firing the IR emitter with current lower than the present 24mA. The amplified signal by the first stage is filtered via high pass filter before being fed to the next stage amplifier and the output of the second stage amplifier is passed through a low pass filter. This will remove all the unwanted frequencies from amplification.

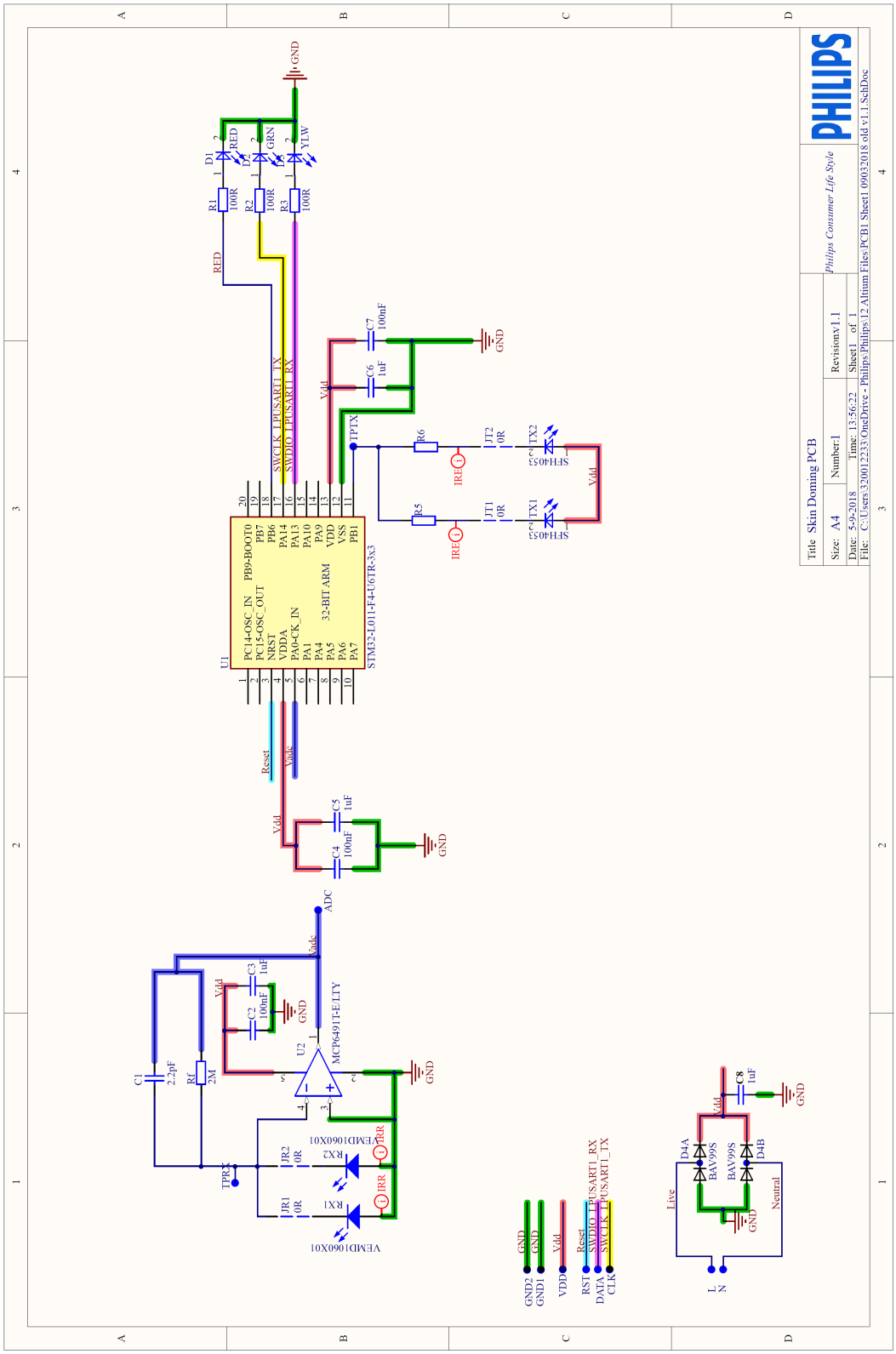

Fig. 5.15 Schematic of version 1 PCB of OMP

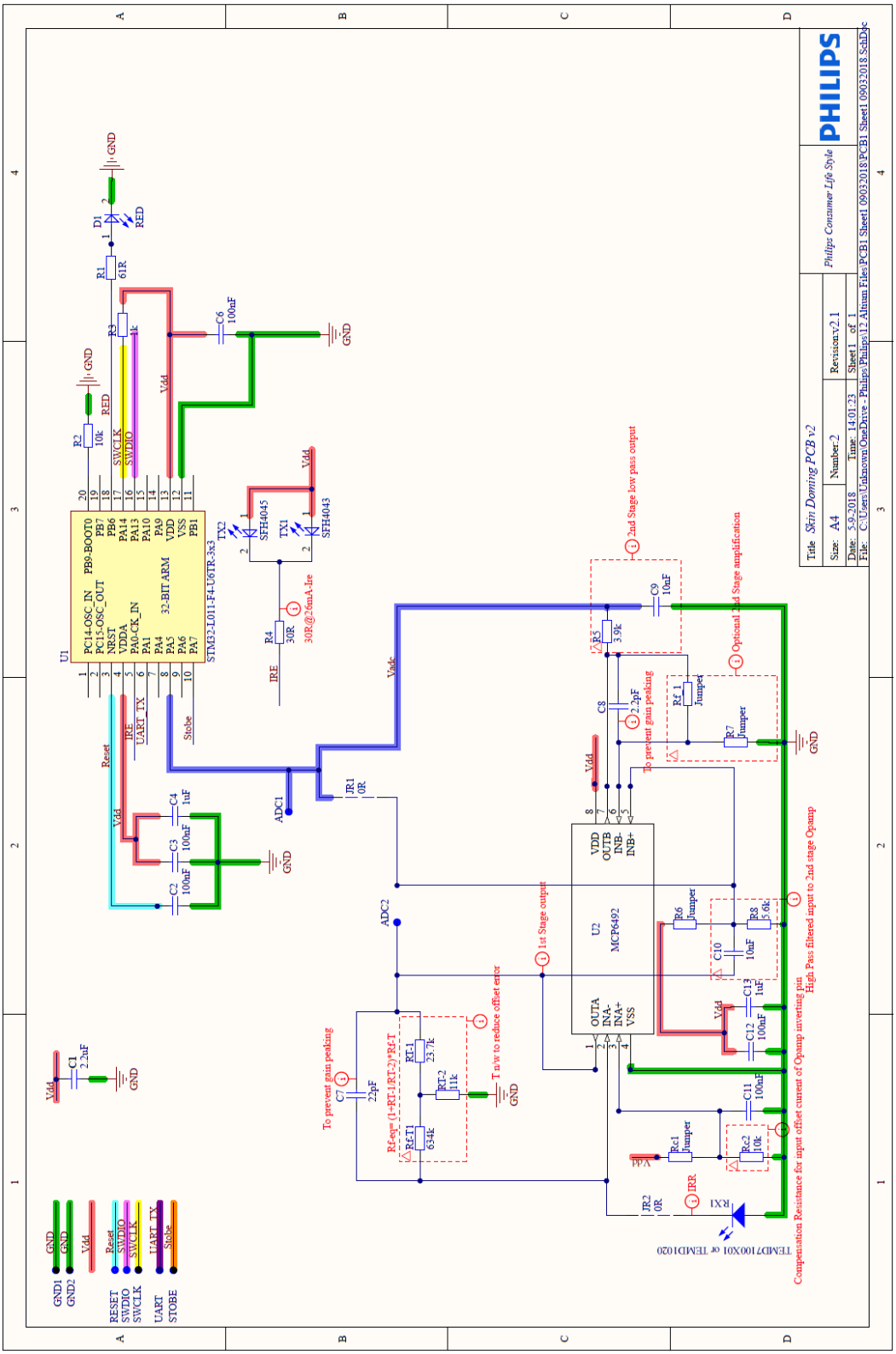

Fig. 5.16 Schematic of version 2 PCB of OMP

Chapter 6

Measurement Algorithm

So far, we have discussed the hardware aspects of the proposed design. But the software aspect of the design is equally important. The software algorithm has to process the received conditioned signal from the signal conditioning circuit in soft realtime. Soft realtime for our design is defined as processed data availability within 3 rotations of the cutter. At highest RPM of 2300 this corresponds to a response time of about 78ms. The Measurement algorithm also is responsible for enforcing power saving measures on the PCB. The prime goal of the algorithm is to identify the slots where skin doming is occurring from a continuous stream of incoming signal data. The algorithm identifies the start of the streaming data on some logic and after encountering the indexing position on the data stream it analyses the data to identify signal corresponding to each slot/hole and if that slot/hole has skin doming occuring. The processed outcome of the data is indexed with the slot/hole positions and sent via uart to a PC for visualization. The visualization is performed using a python script developed by Philips. The graphical user interface shows skin doming in μm in soft realtime.

6.1 Signal Characteristics

Its vital to understand the signal characteristics before explaining the algorithm as it will help to better understand the functionality of the algorithm and its implementation. Fig 6.1 shows the screenshot of the conditioned signal which is being sampled by the microcontroller. The label "Start" indicates the indexing position whose utility is explained in section 6.2.3. The artificial skin is placed between the slots 16 and 34. The signal output corresponding to different parts of the cap is indicted via 1-4 in the

figure. The waveform gets a DC offset as more and more skin is domed in due to the receiver getting stronger reflections.

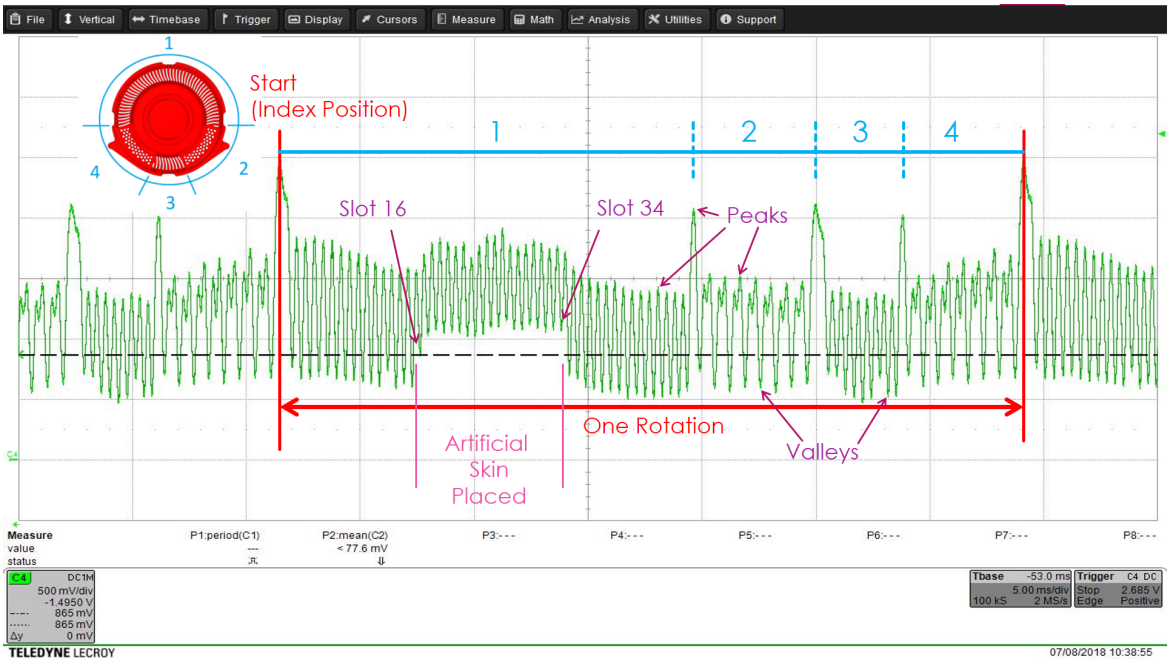

Fig. 6.1 Screenshot of the conditioned signal which is sampled by the microcontroller

6.2 Measurement Algorithm

The measurement Algorithms has the following subsections. Fig 6.2 shows a high level representation of the algorithm.

6.2.1 Initial Configuration

The algorithm starts by configuring the hardware in low power mode. This is achieved by setting the clock to 6MHz internal clock, the ADC is initialised followed by initializing the UART module in low power mode and finally the timer is loaded with value to interrupt at every 70us. The IR emitter is kept switch off during all this configuration. The device is not put into sleep mode during the 70us wait sincethe microcontroller sleep for 70us since effectively this save very little to no power. The algorithm also allocates two arrays ADC_value[502] and ADC_Peaks[151] for buffering the raw and processed signal data.

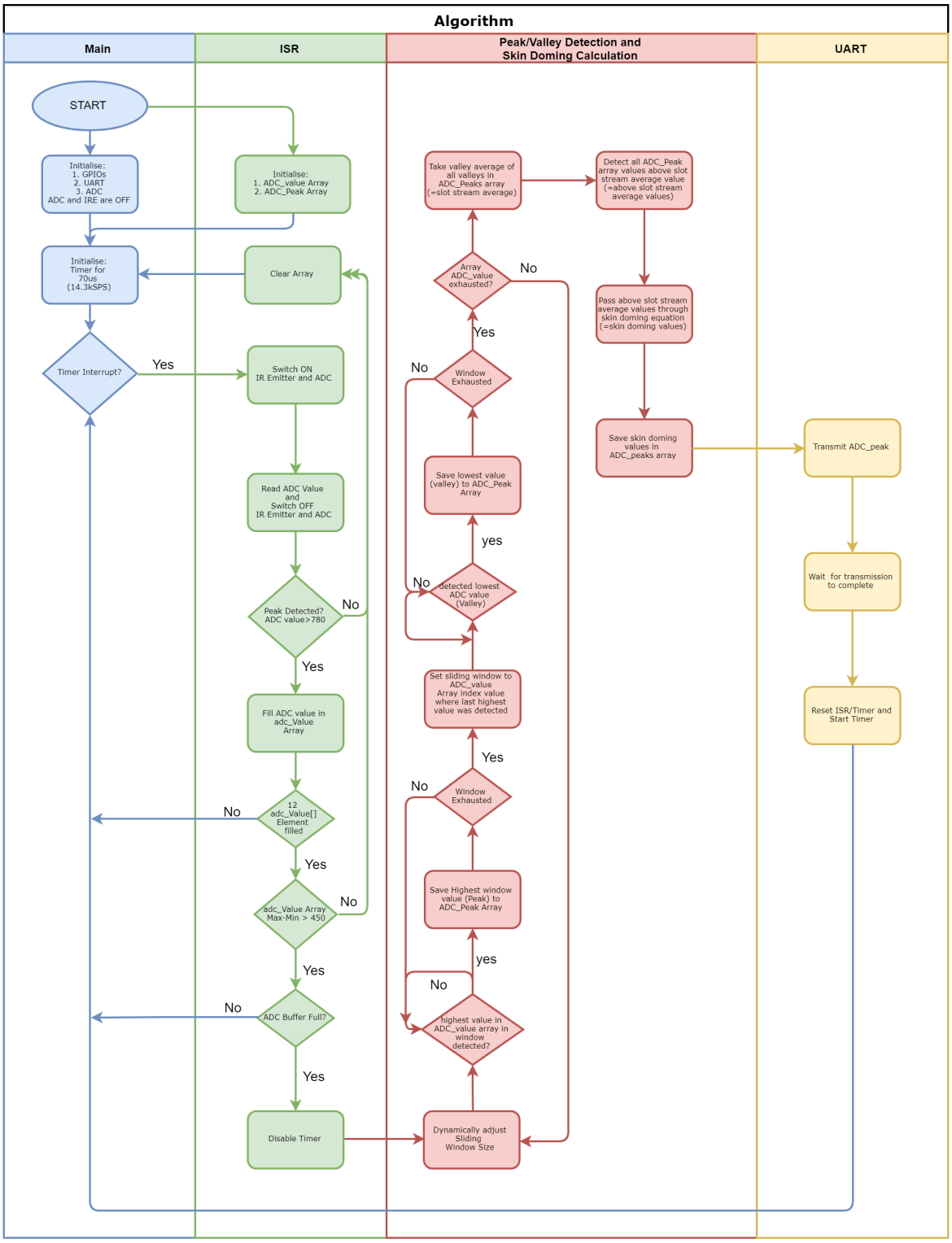

Fig. 6.2 Flowchart of a high level representation of the algorithm

6.2.2 Data Sampling

Immediately after the initialization the timer interrupts every 70us and enters the Interrupt Service Routine (ISR). Every time the program enters the interrupt service routine it reads the value from the ADC register and stores it into the array ADC_value[502]. Since the ISR in serviced every 70us it corresponds to a sampling rate of 14.3kSPS. The justification of choosing the data sampling rate and buffer size is given in table 6.1.

Table 6.1 Sampling rate and array size calculation with worst case RPMs for cutter

Calculations	Cutter RPM		
	Max	Nominal	Min
RPM	2300	2100	1900
RPS	2300/60 = 38.33	2100/60 = 35	1900/60 = 31.67
Time per round	26.0ms	28.6ms	31.5ms
Time per slot/hole	26ms/74 = 351us	28.6ms/74 = 386us	31.5ms/74 = 426us
Sampling time (x5)	351us/5 = 70uS	386us/5 = 77us	426us/5 = 85us
Buffer size at max Sampling rate	26ms/70us = 371	28.6ms/70us = 409	31.5ms/70S = 450
110% of min buffer size at max sampling rate	408	450	495

Hence to prevent and identify buffer overflow (which causes stack overflow), buffer size of 502 was choosen for ADC_value and 151 for ADC_Peaks. The buffer size of ADC_Peaks is based on observation of length of refined data. An even efficient way for ADC sampling is proposed in the chapter 8 which is expected to sample the data only at the physical instant when its most likely to encounter a valley. This would drastically reduce the sampling time and save enormously on power .

6.2.3 Index Position Identification

The algorithm continuously scans the signal data stream for a predefined index position. The index position is defined as the point from where the start of one rotation is counted. This is visible as the label "Start(Index Position)" in fig. 6.1. The algorithm exploits the presence of a distinct signal feature to track the index point. If the algorithm encounters a large ADC value difference between the peak and valley ADC

value within the window size of 12 data points, it starts to buffer the sampled signal data in the ADC_value[502] array. The indexing part of the algorithm hibernates once it detects the correct index position in the signal data stream. The indexing part of the algorithm is reactivated once the complete algorithm ends and data buffering for next cycle is required.

6.2.4 Dynamic Window Sizing and Peak and Valley Detection

Since the RPM of the cutter varies from 1900-2300 RPM, hence keeping a fixed sliding window size to identify the peaks and valleys in the sampled data was not possible. Hence the size of the sliding window is dynamically changed as per the input data stream. Since the signal has a repeatable pattern the algorithm expects a window size readjustment at certain instants. If during that time frame the system encounters a preprogrammed condition it switches the window size. If the condition is not met the window size is not changed. This has proved to be very effective for variations in cutter RPM until the point the RPM or signal quality drastically deteriorates. Dynamic sliding window size modulation helps the system to not miss any valleys or peaks in the signal data stream.

The peak and valley detection part of the algorithm purges all the array data except the data points that define the peaks and valleys within the window size. The peaks and valleys are the highest and lowest ADC value within a sliding window refer fig. 6.1 for peaks and valleys. Since only valleys and peaks hold information about skin doming hence segregation of redundant data from meaning full data is essential. The peak and valley detection part of the algorithm is a modified version of Maxlist algorithm especially developed for this thesis application. This modified version has a dynamic window sizing unlike a fixed window size in Maxlist algorithm [22]. Our algorithm starts from identification of the peak since it is aware that the index point is a peak, it then scans the window size until it encounters the lowest ADC value in the window which is the valley. Once the lowest ADC value is found its resets the window size and starts from the ADC_value array position where it found out the last valley/peak and searches for the next peak/valley respectively. The algorithm checks if window size needs to be changed after certain number of peaks and valleys have been identified.The window size changes for slots and holes, it automatically decides when to change the window size based on the number of valleys identified and if there is a large ADC change which occurs at start of section 2,3 and 4 in fig 6.1. The digitised

output of the conditioned input signal after peak and valley detection is shown and discussed in results and analysis chapter 7 fig. 7.6a .

6.2.5 Skin Doming Calculation

Once the peak and valley values are saved in ADC_Peak array, the skin doming calculation is performed. For the skin doming calculation firstly the algorithm removes all peak values and takes only the average of all valley ADC values (defined as slot stream average). It then compares the ADC_Peak array values with this slot stream average, all values above this slot stream average are passed through an equation which gives the corresponding skin doming in μm. The equation is extracted from the calibration data which is presented in chapter 7. The final processed data in the form of absolute skin doming per slot/hole in μm is stored in ADC_value array.

6.2.6 Data Transmission

Each ADC_value array value is padded with a "$" sign at the start and end of transmission via UART. The GUI interface developed at Philips interprets this "$" sign as start and end of each slot/hole skin doming data. Once the transmission ends the algorithm starts over again.

6.2.7 Power Saving Schemes

Power saving schemes are one of the most critical aspect of this complete design as it intented to be passively powered. Since the total power target with an improved energy harvester prototype is 50mW [18], hence the complete system is expect to operate around 45mW of average power consumption. Since the microcontroller and other associated paraphernalia is already very low power consumption series, not much power can be saved here (just a total of 1-2mW). The bulk power consumption of the earlier design [14] although not explicitly calculated but is expected to be in excess of 225mW, since the emitter was being fired at 70mA of forward current at about 3.3V. Hence IR emitter accounts for the vast majority of power consumption. For this reason focus was given to develop ways to reducing power consumption of IR emitter. Detail analysis of power consumption is disucssed in chapter 7 section 7.2.5.

Pulse Synchronized Measurement

Given the physical layout of the cap and the time taken by the microcontroller to process the data it was decided to fire the IR emitter only when required. This gave birth to the idea of pulse synchronised measurements. The pulse synchronization happens in the interrupt service routine. Pulse synchronization refers to the momentarily pulsing of IR emitter only when required. The algorithm doesn't fire the IR emitter continuously but just before it needs to take an ADC sample. Rest of all the time the IR emitter is switched off. This approach has resulted in drastic reduction in power consumption of the IR emitter results of which are discussed in the next chapter 7.

Chapter 7

Results and Analysis

The goals, deliverables and design requirements set forward for this thesis in section 1.5 have been discussed in this chapter. So far, we have discussed the design and implementation of the proposed method to measure skin doming. This chapter will present and validate the claims of the design. Please note that since no similar research has been done in this area of integrating optical sensors inside a shaver head, the results and finding of this chapter may be the only available reference standard.

7.1 Skin Doming Measurements

Certain amount of pressure while shaving is absolutely essential to have a good shave, this small pressure is sufficient until too much of skin doming occurs. Since the thickness of the shaving cap lamella is ≈60μm hence skin doming until 60μm is permissible.

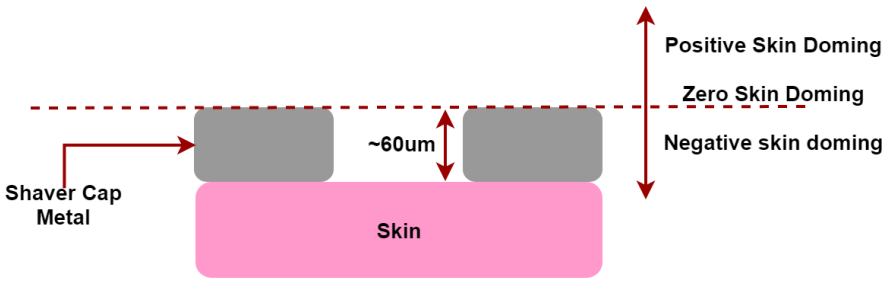

Fig. 7.1 Cross sectional view of skin doming though the metal cap, showing the approximate thickness of shaving cap lamella and defining boundaries for zero, positive and negative skin doming.

The skin doming above 60μm is prone to be cut by the cutter. With this understanding the skin doming has been defined as "Positive skin doming" , "Negative skin doming" and "Zero skin doming". Fig. 7.1 illustrates the physical significance of the above definitions.

With reference to the above mentioned details, measurements for different amount of skin doming for different readings of micro screw gauge were taken using the setup described in section 4.4. Graphs 7.2a and 7.2b illustrate skin doming measured under the OCT machine at slots and holes respectively. They show the relationship between the skin doming at the slots or holes and the micro screw gauge readings. Since one of the design goal M.2 in section 1.5.2 was to measure skin doming at each slot , hence skin doming measurements were taken for forward run i.e micro screw gauge displacement from 5.5mm to 4.3mm and a reverse run i.e from 4.3mm to 5.5mm. Micro screw gauge readings above 4.3mm were not taken as depression in the metal shaving cap could be seen under the OCT machine, indicating too much pressure.

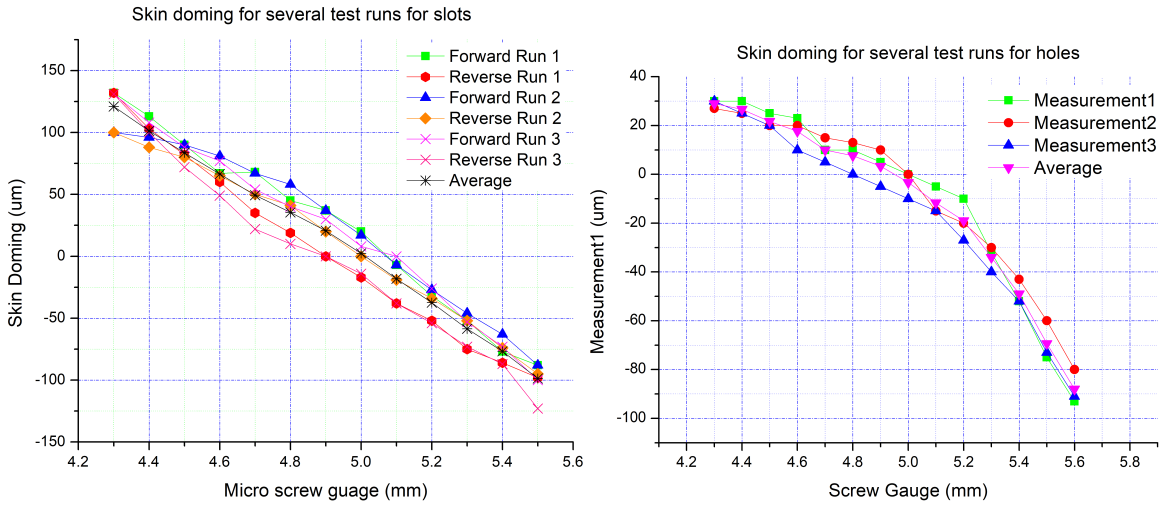

(a) (b)

Fig. 7.2 Figure (a) shows skin doming at slots as measured on OCT machine for different readings of micro screw gauge and (b) shows skin doming at holes as measured on OCT machine for different readings of micro screw gauge.

As evident from graphs 7.2a and 7.2b that the reading of skin doming under the OCT for the reverse run does not trace back the readings obtained in the forward run. This is more evident from graph 7.3 which illustrates the hysteresis by plotting the average of all forward runs and the average of all reverse runs.

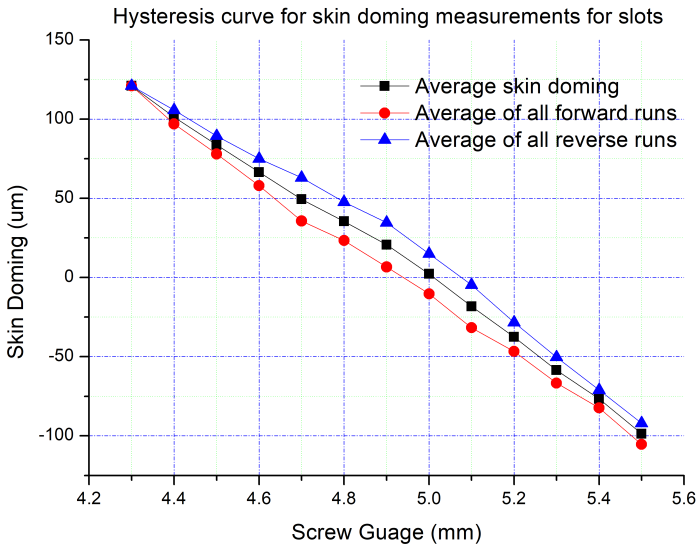

Fig. 7.3 Hysteresis curve for measured skin doming for slots under OCT for several forward and reverse runs.

For the purpose of our calculations the average skin doming of the hysteresis curve was taken. These average skin doming values are taken for all further calculations used in interpretation of data obtained from OMP. Some of the possible causes for the hysteresis are mentioned in the following section.

7.1.1 Measurement Tolerances

In this section factors affecting the calibration measurements are discussed. Following are the factors that were considered while making the measurements.

OCT Measurement

The measurement resolution for the OCT machine is 5μm. The resolution of the image displayed on the computer screen of the OCT machine is 5μm/pixel, hence misjudgement of the end of skin doming edge on the grainy screen image (refer fig. 4.9) can result in an error of $\pm$5μm .

Plasticity of Artificial Skin

The artificial skin tends to deform and take the shape of the slots and holes, this causes low skin doming initially but as the skin is pushed more and more into the metal shaving cap it takes the shape of the slot/hole. This is evident when the translation

table is moved in the reverse direction. The amount of skin doming for the reverse motion of the translation table shows a deviation of up to 20 μm from the readings taken during the forward motion of the translation table.

Backlash of Micrometre Screw Gauge

The mismatch or hysteresis in the skin doming readings for the forward and reverse motion of the translation table is also because of the backlash of the microscrew gauge. This is again an unavoidable measurement error while using such an assembly.

Observational and Approximation Error

The readings of the microscrew gauge and on the OCT machine images on the computer are subjective to human interpretation and approximation errors. Although utmost care has been taken to avoid such errors, still the measurements are prone to such errors.

7.2 OMP and Algorithm Measurement Results

7.2.1 Data Sampling Results

The average skin doming data at the slots for different displacement of micro screw gauge from fig. 7.3 needs to be cross-interpreted with respect to ADC values. This is done by means of the test assembly as discussed in section 4.4 fig. 4.8. Using the mentioned test assembly the OMP was placed inside the shaver cap with the artificial skin placed between slot 16 and 34. As the shaver was switched on, the OMP rotated and the conditioned sensor signal was captured by means of slip ring assembly as shown in fig. 4.11 at the oscilloscope and saved. The captured waveform from the OMP is again shown in fig 7.4 for easy reference. The micro screw gauge was again moved to the same positions as shown in fig 7.2a and the waveforms were recorded.

Due to the unbalanced rotation of the OMP in the shaver, the waveforms were polluted with a lot of noise due to the mechanical vibrations which affect the sensor reading. For this reason clean portions of the waveform for different amount of skin doming were recorded using the oscilloscope and are fed into the OMP to measure skin doming by regeneration using an arbitrary function generator. The clean signals recorded by the oscilloscope for different amount of skin doming were fed into the OMP. The optical measuring platform digitised the recorded signal fed from the arbitrary

function generator at 14.3kSPS sampling rate. The resulting high fidelity digitised waveform is show in fig. 7.5. Its evident on comparison with fig. 7.4 that the digitised waveform is a replica of the original analogue signal, validating the optimal sampling rate calculations in table 6.1.The digitised waveform as shown in fig. 7.5 is buffered inside the array ADC_values. All post processing is done on this data array and the results are discussed in the following section.

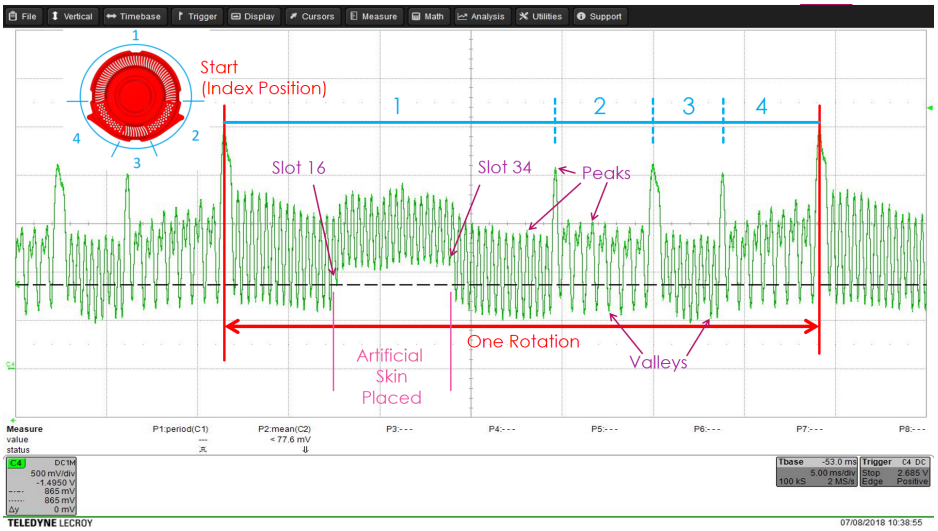

Fig. 7.4 Screenshot of the conditioned signal which is sampled by the microcontroller.

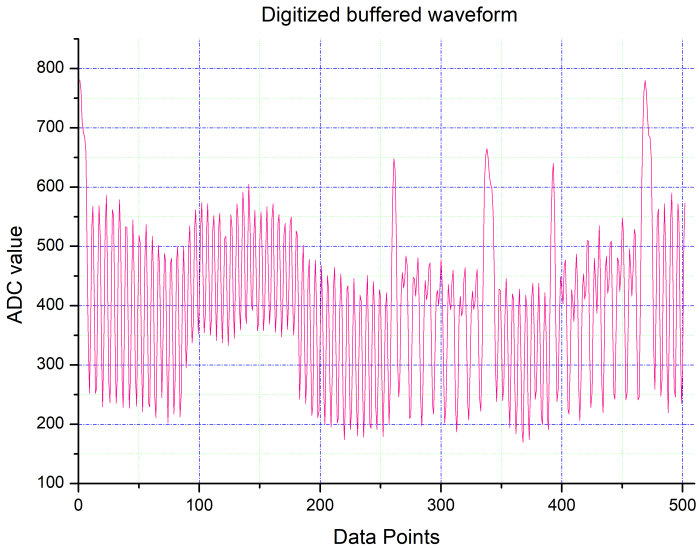

Fig. 7.5 Digitised waveform by OMP at 14.3kSPS.

7.2.2 Algorithm Data Processing Results

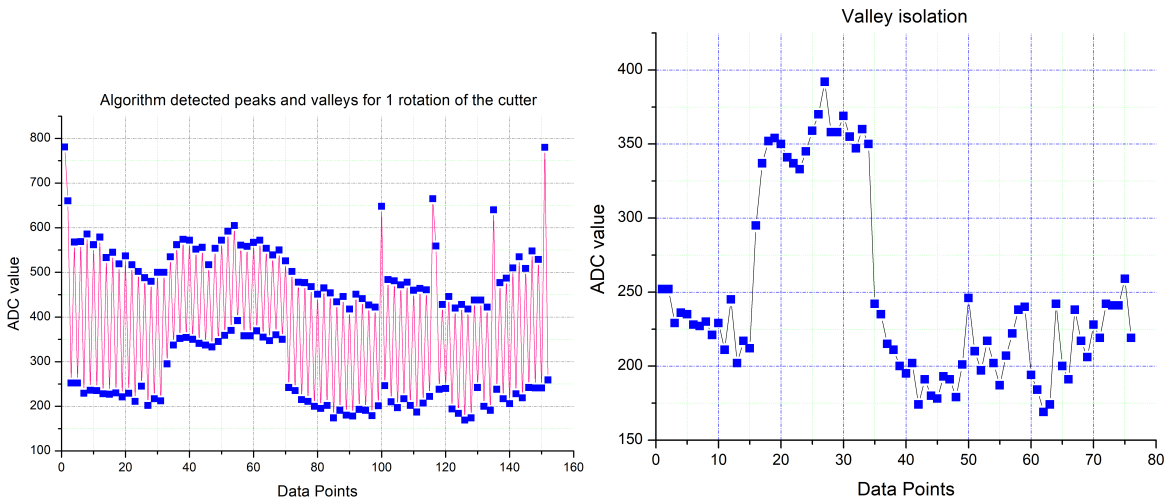

(a) (b)

Fig. 7.6 Figure (a) shows peaks and valley detection for digitised waveform and (b) shows valley ADC value isolation.

The buffered digitised waveform is processed as per the algorithm discussed in chapter 6. The algorithm isolates the peaks and valleys and discards the rest of the ADC values in the array refer fig. 7.6a.

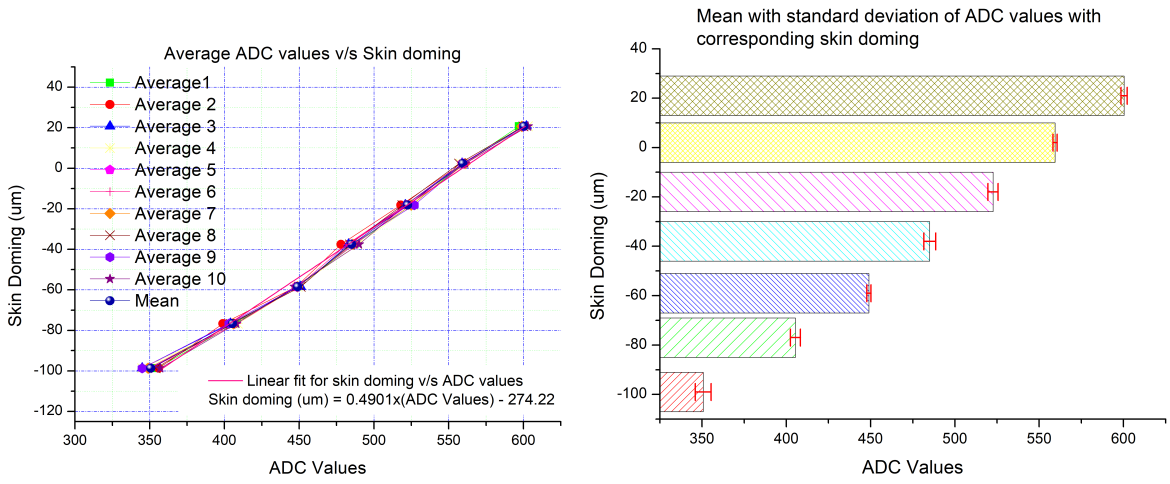

(a) (b)

Fig. 7.7 Figure (a) shows measured average ADC values for differnt amounts of skin doming over several slots and (b) shows mean and standard deviation of average skin doming measured on the slots using the OMP.

In the next step the algorithm removes the peaks and only the ADC values representing the valleys as shown in fig. 7.6b. An average of 10 runs is taken for all valleys with different amounts of skin doming. The mean of the average values is taken as shown in fig. 7.7a. The mean and standard deviation of these average values are shown in fig. 7.7b. Based on the mean of the average ADC values for different amount of skin doming a linear curve was fit. This linear curve equation is as given below:

$$Skin\ doming(um) = 0.4901 \cdot (ADC\ value) - 274.22 \tag{7.1}$$

This equation is the essence of the whole measuring system. This equation related directly the measured ADC value to the amount of skin doming in μm. The measured amount of skin doming for each individual slot is represented in a GUI, which fulfils the goal A.1 of section 1.5. The screenshot of the GUI with the measured skin doming is shown in fig. 7.13 at the end of the chapter.

7.2.3 Skin Doming Measurement Accuracy

Validation of measurement accuracy to be within 10μm as specified in goal M.1 in section 1.5, is not feasible since the OCT machine's skin doming measurements were carried out for only one slot. In practicality skin doming will not be the same across all slots , neither will it be exactly equal to what was measured under the OCT machine. The skin doming measurement algorithm works on the approach of measuring average ADC values for the skin doming occurring over several slots. With no clear means to ascertain the accuracy of measurement by the OMP with respect to the OCT machine measurement simultaneously while the shaver is in operation, brings the accuracy of measurement of the proposed system in a grey area.

Thus it was decided to mathematically analyse the accuracy. As per requirement of M.1 error upto 10μm is permitted, for equation 7.1 it means that an ADC error of upto 20 ADC values. This brings us back to the graph 7.7b, the maximum deviation of ADC values occurs at -100μm , which is 4.69, table 7.1 attached at end of this chapter shows the standard deviation values for the graph 7.7b. For the table the maximum difference can be $\pm 5 ADC values$. This according to equation 7.1 for the maximum swing of 10 ADC values the maximum swing in the measured skin doming can be

$$0.4901 \times 355 - 274.22 - \Big(0.4901 \times 345 - 274.22\Big) \simeq 5um$$

This value of 5μm is within the design requirement of M.1 in section 1.5.

7.2.4 Response Time

The measurement goal M.3 set in section 1.5 specifies the response time of 78ms for the skin doming measurement to complete. This design goal is met since the a response time of proposed design is 66ms as visible in fig. 7.9.

7.2.5 Power Consumption

The next focus of the design analysis is the power consumption. The total available power budget is about 45mW. This section shows a breakdown of the power consumption calculations and measurements for different modules of the system, namely, the sensor system, the microcontroller and the signal conditioning unit. A comparison of power consumption with and without the power saving schemes is also analysed.

Sensor System Power Consumption

Fig. 7.8 Mean power consumption of 81.2mW without pulse synchronised power saving scheme.

The forward voltage drop of the IR emitter is 2.4V hence with 3.2V supply voltage (actual supply voltage in the design) and 32Ω (i.e 30Ω current limiting resistor for IR

emitter+ 2Ω soldering and contact resistance) resistance the current consumption of the IR emitter comes out to be 25mA which is just within limits of the current sinking capability of the GPIO. This translates to a power consumption of 81.2mW alone for the sensor system. This is also evident from fig. 7.8.

This much power consumption is not feasible with an energy harvester with a peak power delivery capacity of 50mW. Hence, power saving schemes as discussed in section 6.2.7 are implemented. Under these schemes the IR emitter is pulse synced with the ADC sampling rate, which allows the emitter to fire just before the ADC sampling instant and remain switched off for the remaining time. This pulse synchronised operation with ADC sampling rate of 14.3kSPS (or 70us sampling time) is implemented and it resulted in reducing power consumption by 38.64mW. This brings the total power consumption of the system to 42.56mW as visible from fig. 7.9. This is well within the design goal A.2 in section 1.5.

Fig. 7.9 Reduced mean power consumption by 38.64mW or about 48% with pulse synchronised power saving scheme.

Microcontroller Power Consumption

The microcontroller power consumption is calculated using the microcontroller power consumption calculator from ST Microelectronics. The simulated power consumption performance is done for a system clock frequency of 6MHz with the required peripherals switched on. The combined current consumption of 1.12mA for all the peripherals is given in fig. 7.10, this gives an equivalent power consumption of 3.6mW at 3.2V supply voltage.

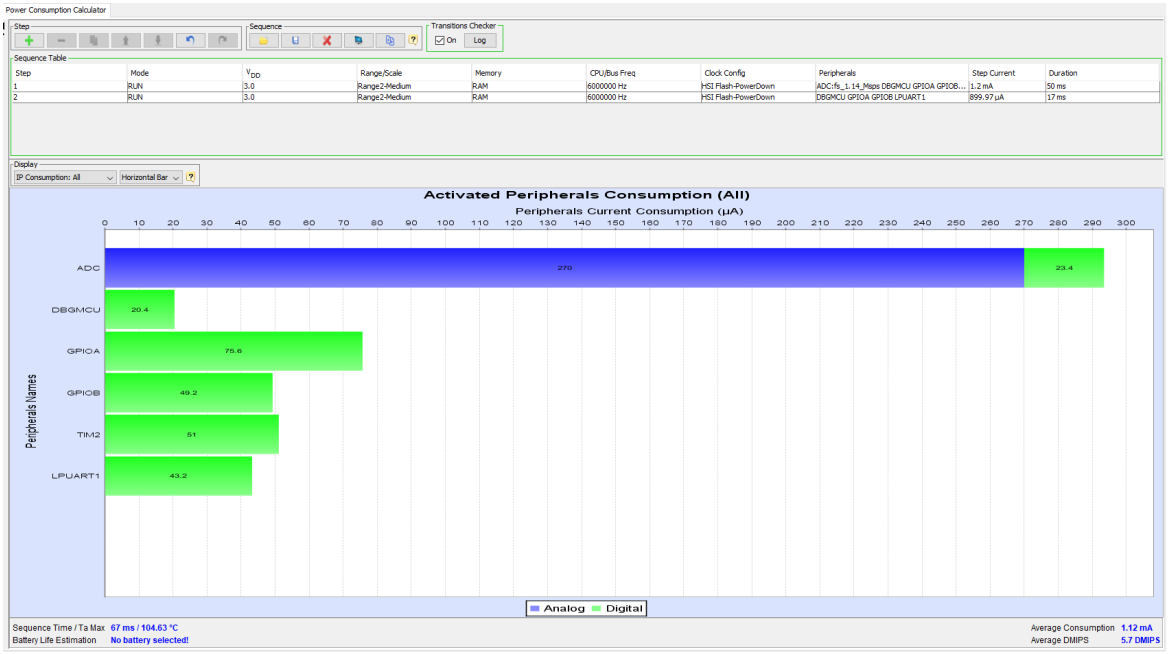

Fig. 7.10 Combined power consumption of all peripherals.

From the graph we see that the majority of the current is consumed by the ADC sampling in the microcontroller. Presently the system is sampling at 5x the required frequency , but if the ADC sampling could be perfectly synchronised with the slots as discussed in section 4.3.3 fig. 4.6, the current consumption of the ADC is expected to go down with the same factor, which would be a considerable power saving for the microcontroller.

Signal Conditioning Circuit Power Consumption

The power consumption of the opamp signal conditioning circuit as shown in fig. 5.8 is calculated by simulation using an LTspice model of the opamp MCP6491 imported from the manufacturer's website. The simulated current consumption at

3.2V DC is approximately 521μA which is in line with the datasheet specification for current consumption of the opamp, the results are shown in fig. 7.11. Hence the power consumption of the signal conditioning circuit at 3.2V is ≈1.7mW.

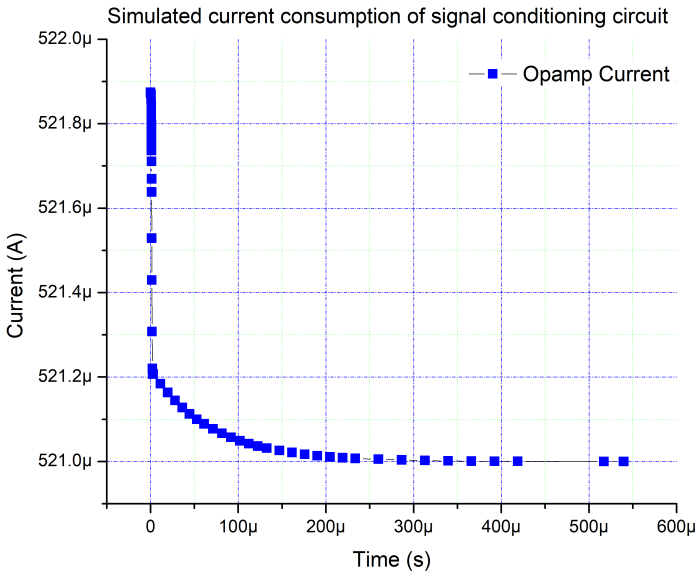

Fig. 7.11 Current consumption of signal conditioning circuit as shown in fig. 5.8.

7.2.6 Combined Power Consumption Overview

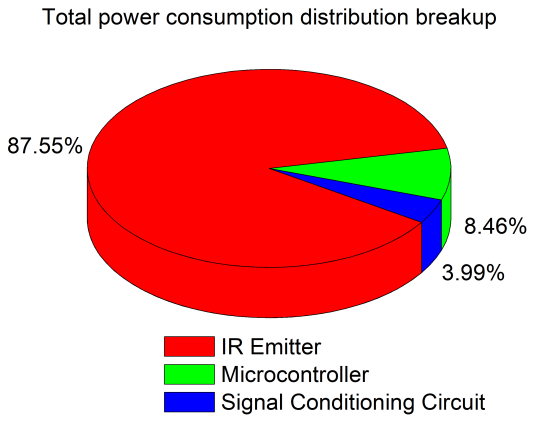

Fig. 7.12 Power consumption share of different modules.

From the power analysis we see that the power consumption of the sensor system is the majority stake holder with 87.55% of the total power consumption of the OMP. The microcontroller and signal conditioning circuit take up 8.46% and ≈4% respectively. This indicates that the signal conditioning circuit's and microcontroller's power consumption is negligible in comparison to power consumption of the sensor system. Thus, for future improvements the focus should be on further reducing power consumption of the sensor system.

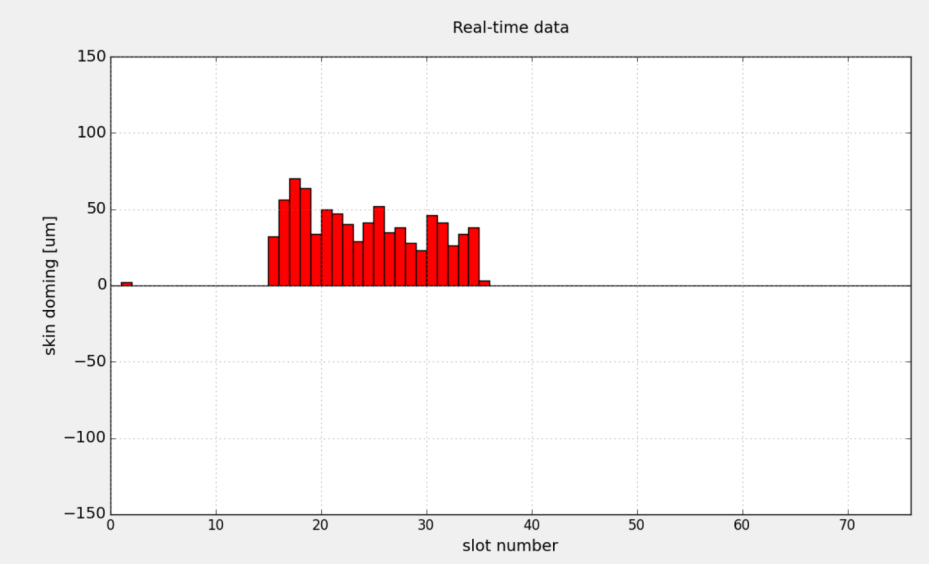

Fig. 7.13 GUI for data visualization. Showing positive skin doming with respect to each slot.

Table 7.1 Mean and standard deviation for ADC measurements for different skin doming.

Skin Doming in um	ADC Average											
	Run1	Run2	Run3	Run4	Run5	Run6	Run7	Run8	Run9	Run10	Mean	Std Dev
-99	355	356	345	345	350	351	349	354	345	357	350.70	4.69
-77	407	399	404	409	406	408	406	404	403	408	405.40	2.99
-59	449	448	451	449	448	449	449	451	449	447	449.00	1.25
-38	487	478	483	489	487	482	486	484	485	490	485.10	3.54
-18	525	518	521	526	523	521	525	519	527	521	522.60	3.06
2	560	559	559	558	559	560	561	557	560	561	559.40	1.26
21	597	600	602	603	600	600	599	600	600	603	600.40	1.84

Chapter 8

Conclusion and Future Work

In this thesis an attempt was made to develop an integrated self-contained stand alone low power system to measure linear displacement in the form of skin doming with a few μm accuracy. This thesis has contributed in creating the first prototype of the system which can actually fit in the cutter with minimal modifications to the present assembly of the shaver. Hopefully it will evolve into a full fledged product, both for test engineers and end consumers. A detailed summary of outcomes and future extension of this work is mentioned in the following sections.

8.1 Summary of Outcomes

The result and outcomes of this thesis are compared with the initial goals and deliverables set in chapter 1 section 1.5 and are presented as follows:

8.1.1 Design Goals

The design constrain of area limitation of $2cm^2$ for the PCB is complied with, the total area of the developed PCB comes out to be $1.82cm^2$. The proposed design also fits into the existing cutter assembly with minimal changes to the existing hardware. Thus the proposed design meets all design goals.

8.1.2 Measurement Goals

The measurement goal was set to an accuracy of 10μm, in this regard mathematical analysis calculated the deviation in measurement accuracy due to ADC measurement error which comes out to be approx. 5μm. This may appear to be a satisfying figure

but measurement tolerances and inaccuracies as mentioned in section 7.1.1 may cause deviation in actual measurement accuracy. This needs to be further investigated. The measurement of skin doming is possible at each slot and hole of the shaver cap as initially set in the measurement goals. The skin doming for each slots is measured and shown in the GUI.

The soft real-time performance was defined by specifying the time limit for measurement to be within 78ms (which corresponds to time for three rotation at 2300RPM), but the proposed design out performs the set requirements by 12ms. The measurement is completed in 66ms.

8.1.3 Analysis Goals

The measured data is presented in the GUI. The GUI is an adaptation of an existing GUI used at Philips, the interface is very basic but fulfils the analysis requirement of being able to visualise the amount of skin doming on each slot. The power constrain requirements of the design were the most stringent, the proposed design just manages to accommodate its power budget within 45mW. The pulse synchronised ADC sampling and other power saving schemes saves about 48% power in comparison to continuous unsynchronised ADC sampling which took about 81mW of power. The total power consumption of the system with pulse synchronised ADC sampling is 42.56mW. But this power consumption is still too close to the absolute rating of the proposed energy harvester with almost no room to spare power for any transient power spikes, these transient peak power requirements can cause issues with the energy harvester and system performance.

8.1.4 Documentation Goals

The documentation goals have been satisfied in the form of this thesis.

8.2 Future Extension of the Work

Although the present work meets or exceeds all design specification, goals and deliverables set for this thesis, but it leaves some loose ends and unanswered questions. These recommendations and deficiencies can be addressed in the future extension of this work.

8.2.1 Improvements in Mechanical Assembly

The design of mechanical assembly remains one of the most critical part of this work. Due to the sensor system being in a very primitive stage, a lot of time was spent on the development of mechanical assembly for the system. But due to lack of expertise in the field of mechanical engineering, unfortunately the proposed design could not be tested in the actual system due to mechanical bottlenecks of the developed mechanical assembly. The unbalanced rotation of the measuring assembly inside the cap results in introduction of a lot of mechanical vibrations in the sensor assembly. These mechanical vibrations cause measurement inaccuracies in the sensors assembly. To be able to test the design in actual cutter, more of mechanical and precision engineering is needed to develop a more reliable well balanced and precise mechanical assembly for the sensor.

8.2.2 Synchronised Data Sampling

Although the design barely manages to meet the power requirement goals of the thesis, but there is more scope for improvements. To further improve the power efficiency we need to look back at the pie chart 7.12, which indicates that majority of power is consumed by the IR emitter. Hence a perfectly synchronised ADC sampling with the slots and holes is needed. This is discussed in section 4.3.3, if this is implemented then the power consumption of IR emitter should go down by a factor of 5. Which should result in a huge power saving.

8.2.3 Sleep Mode for Microcontroller

Due to high sampling rates of 14.3kSPS or 70μs, the microcontroller barely gets any time to sleep and saves almost no power. Hence sleep mode was not implemented but if improvements in data sampling can be made as discussed in the previous subsection, the microcontroller will get sufficient time to sleep and save on power.

8.2.4 Skin Doming Measurement at Holes

Since the goals of the thesis didn't require measurement to be made for the skin doming at holes, hence it was left unattended but future implementation can also measure skin doming at the holes.

8.2.5 RPM Feedback

RPM feedback is a nice to have feature of the design. Presently Fluke contact-less LED strobe-scope is used to measure RPM of the cutter. But the proposed design with some changes in the algorithm can also measure RPM very accurately in almost real-time, there-by removing the use of strobe-scope which is inaccurate and time consuming to use.

8.2.6 Cleaning of the Sensor

Till now no attempts have been made to identify more practical problems of the present approach of using optical sensors to measure skin doming. The performance of the system needs to be investigated once the optical sensor assembly gets polluted and contaminated with shaving foam and water. In future, modifications can be made to self clean the optical sensor while rotating in the cutter. Polishing by rotation perhaps works as the FOC appeared to have improved surface finish after rotating inside the cap, but this needs to be investigated.

References

[1] Estibaliz Asua et al. “A Novel Micro- and Nano-Scale Positioning Sensor Based on Radio Frequency Resonant Cavities”. In: *Sensors* 14.6 (2014), pp. 9615–9627. DOI: 10.3390/s140609615. URL: https://www.ncbi.nlm.nih.gov/pubmed/24887041.

[2] Kenneth Flamm. “Measuring Moore’s Law: Evidence from Price, Cost, and Quality Indexes”. In: (Nov. 2017). DOI: 10.3386/w24553. URL: https://www.imf.org/~/media/Files/Conferences/2017-stats-forum/session-6-kenneth-flamm.ashx.

[3] Thad Starner Bernard Kress. “A review of head-mounted displays (HMD) technologies and applications for consumer electronics”. In: *Proc.SPIE* 8720 (2013), pp. 8713–8720. DOI: 10.1117/12.2015654. URL: https://doi.org/10.1117/12.2015654.

[4] Y. Ding et al. “Distributed Sensing for Quality and Productivity Improvements”. In: *IEEE Transactions on Automation Science and Engineering* 3.4 (Oct. 2006), pp. 344–359. ISSN: 1545-5955. DOI: 10.1109/TASE.2006.876610. URL: https://ieeexplore.ieee.org/document/1707953/.

[5] *Global Market Study on Shavers: Electric Shavers Product Type Segment to Dominate in Terms of Market Share During 2017 - 2025*. Sept. 2017. URL: https://www.persistencemarketresearch.com/market-research/shavers-market.asp.

[6] *How To Get A Good Clean Shave Without Razor Burn*. Oct. 2014. URL: http://www.thebrunettediaries.com/how-to-get-a-good-clean-shave-without-razor-burn.

[7] M. R. Freeman. “Principles and applications of ultrafast magneto-optic sampling”. In: 2 (Nov. 1997), 234–235 vol.2. ISSN: 1092-8081. DOI: 10.1109/LEOS.1997.645383. URL: https://ieeexplore.ieee.org/document/645383/.

[8] E. A. Margatskaya and D. A. Kurnosov. “Differential Optical sensor for measuring small linear displacement”. In: (May 2017), pp. 1–4. DOI: 10.1109/ICIEAM.2017.8076378. URL: https://ieeexplore.ieee.org/document/8076378/.

[9] B. George, Z. Tan, and S. Nihtianov. “Advances in Capacitive, Eddy Current, and Magnetic Displacement Sensors and Corresponding Interfaces”. In: *IEEE Transactions on Industrial Electronics* 64.12 (Dec. 2017), pp. 9595–9607. ISSN: 0278-0046. DOI: 10.1109/TIE.2017.2726982. URL: https://ieeexplore.ieee.org/document/7979582/.

[10] Paul Regtien and Edwin Dertien. *Sensors for Mechatronics (Second Edition), Chapter 7 - Optical sensors*. Elsevier, 2018, pp. 183–243. ISBN: 9780128138113. DOI: https://doi.org/10.1016/B978-0-12-813810-6.00007-0. URL: http://www.sciencedirect.com/science/article/pii/B9780128138106000070.

[11] Byoungho Lee. "Review of the present status of optical fiber sensors". In: *Optical Fiber Technology* 9.2 (2003), pp. 57–79. ISSN: 1068-5200. DOI: https://doi.org/10.1016/S1068-5200(02)00527-8. URL: http://www.sciencedirect.com/science/article/pii/S1068520002005278.

[12] Andreas Othonos. "Fiber Bragg gratings". In: *Review of Scientific Instruments* 68.12 (1997), pp. 4309–4341. DOI: 10.1063/1.1148392. eprint: https://doi.org/10.1063/1.1148392. URL: https://doi.org/10.1063/1.1148392.

[13] A. Vallan et al. "Two-Dimensional Displacement Sensor Based on Plastic Optical Fibers". In: *IEEE Transactions on Instrumentation and Measurement* 62.5 (May 2013), pp. 1233–1240. ISSN: 0018-9456. DOI: 10.1109/TIM.2012.2236725.

[14] Johan Bramer. "Measuring the amount of skin doming by integrating a sensor based system into an electric rotary shaving". Bachelor's Thesis. 2018.

[15] Y. Ran et al. "Vibration Fiber Sensors Based on SM-NC-SM Fiber Structure". In: *IEEE Photonics Journal* 7.2 (Apr. 2015), pp. 1–7. ISSN: 1943-0655. DOI: 10.1109/JPHOT.2015.2408436. URL: http://ieeexplore.ieee.org/document/7053907/.

[16] Vishay Semiconductors. *TEMD7100X01*. Oct. 2011. URL: https://www.vishay.com/docs/81960/temd7100.pdf.

[17] Osram Opto Semiconductors. *CHIPLED® with High Power Infrared Emitter (940 nm), Version 1.4*. June 2017. URL: https://www.osram.com/media/resource/hires/osram-dam-2496058/SFH%204043.pdf.

[18] Jelmer W. Brinkman and Ruben van der Vaart. "Digital Shave Enhancement Energy harvesting". Bachelor's Thesis. 2018.

[19] Thijs Ronda. "Logic Outputs as Rectifier for Energy Harvesting". Bachelor's Thesis. 2018.

[20] Patrick Lichtsteiner, Christoph Posch, and Tobi Delbruck. "A 128×128 120 dB 15 μs Latency Asynchronous Temporal Contrast Vision Sensor". In: *IEEE Journal of Solid-State Circuits* 43.2 (2008), pp. 566–576. DOI: 10.1109/jssc.2007.914337. URL: https://ieeexplore.ieee.org/document/4444573/.

[21] Jae-Yeon Won et al. "Proximity sensing based on a dynamic vision sensor for mobile devices". In: *IEEE Transactions on industrial electronics* 62.1 (2015), pp. 536–544. URL: https://ieeexplore.ieee.org/abstract/document/6847682/.

[22] S. C. Douglas. "An efficient algorithm for running max/min calculation". In: *1996 IEEE International Symposium on Circuits and Systems. Circuits and Systems Connecting the World. ISCAS 96*. Vol. 2. May 1996, 5–8 vol.2. DOI: 10.1109/ISCAS.1996.540338. URL: https://ieeexplore.ieee.org/document/540338/.

[23] Bartlomiej Guzowski and Mateusz Lakomski. "Realization of fiber optic displacement sensors". In: *Optical Fiber Technology* 41 (2018), pp. 34–39. URL: https://www.sciencedirect.com/science/article/pii/S1068520017306211.

[24] Cefu Hong and Soichi Ibaraki. "Non-contact R-test with laser displacement sensors for error calibration of five-axis machine tools". In: *Precision Engineering* 37.1 (2013), pp. 159–171. URL: https://www.sciencedirect.com/science/article/pii/S0141635912001298.

[25] Zhouxiang Jiang et al. "On-machine measurement of location errors on five-axis machine tools by machining tests and a laser displacement sensor". In: *International Journal of Machine Tools and Manufacture* 95 (2015), pp. 1–12. URL: https://www.sciencedirect.com/science/article/pii/S0890695515300420.

[26] Francisco J Azcona et al. "A nanometric displacement measurement system using differential optical feedback interferometry". In: *IEEE Photonics Technology Letters* 25.21 (2013), pp. 2074–2077. URL: http://ieeexplore.ieee.org/document/6595025/.

[27] Sha Xia and Stoyan Nihtianov. "Capacitive sensor system for sub-nanometer displacement measurement". In: *Sensors, 2011 IEEE*. IEEE. 2011, pp. 1173–1176. URL: https://ieeexplore.ieee.org/iel5/6114955/6126898/06127328.pdf.

[28] KR Sandra, Boby George, and V Jagadeesh Kumar. "A novel variable reluctance-hall effect transduction technique based displacement sensor". In: *Instrumentation and Measurement Technology Conference (I2MTC), 2017 IEEE International*. IEEE. 2017, pp. 1–5. URL: http://ieeexplore.ieee.org/document/7969815/.

[29] Sheng-Ming Yang and Chien-Lung Huang. "A hall sensor-based three-dimensional displacement measurement system for miniature magnetically levitated rotor". In: *IEEE Sensors Journal* 9.12 (2009), pp. 1872–1878. URL: https://ieeexplore.ieee.org/iel5/7361/5290388/05291947.pdf.

[30] Wei Gao and Satoshi Kiyono. "High accuracy profile measurement of a machined surface by the combined method". In: *Measurement* 19.1 (1996), pp. 55–64. URL: https://www.sciencedirect.com/science/article/pii/S0263224196000668.

[31] Zi-qiang Yin and Sheng-yi Li. "Exact straightness reconstruction for on-machine measuring precision workpiece". In: *Precision engineering* 29.4 (2005), pp. 456–466. URL: https://www.sciencedirect.com/science/article/pii/S0141635905000498.

[32] SW Harun et al. "Fiber optic displacement sensors and their applications". In: *Fiber Optic Sensors*. InTech, 2012. URL: http://cdn.intechopen.com/pdfs/29114/InTech-Fiber_optic_displacement_sensors_and_their_applications.pdf.

[33] Mohd Zulhakimi Ab Razak et al. "Noncontact optical displacement sensor using an adiabatic U-shaped tapered fiber". In: *IEEE Sensors Journal* 15.10 (2015), pp. 5388–5392. URL: https://ieeexplore.ieee.org/iel7/7361/7181761/07095531.pdf.

[34] Sahil Khubchandani, Melinda R Hodkiewicz, and Adrian Keating. "Characterizing the Performance of LED Reflective Distance Sensors". In: *IEEE Access* 5 (2017), pp. 14289–14297. URL: https://ieeexplore.ieee.org/document/7990492/.

[35] Karolina Orłowska et al. "Light intensity fibre optic sensor for MEMS displacement and vibration metrology". In: *Optics & Laser Technology* 65 (2015), pp. 159–163. URL: https://www.sciencedirect.com/science/article/pii/S0030399214001996.

[36] Yusuke Kanzawa, Yoshikatsu Kimura, and Takashi Naito. "Human skin detection by visible and near-infrared imaging". In: *IAPR Conference on Machine Vision Applications*. Vol. 12. Citeseer. 2011, pp. 14–22. URL: http://citeseerx.ist.psu.edu/viewdoc/download?doi=10.1.1.389.6745&rep=rep1&type=pdf.

[37] *Photodiode Characteristics and Applications*. URL: http://www.phas.ubc.ca/~beaudoin/PDS%20Papers/Position%20Detector%20Info/UDT_PhotodiodeCharacteristics.pdf.

[38] Yang Zhen. *AN1494 - Using MCP6491 Op Amps for Photodetection Applications*. Nov. 2012. URL: http://ww1.microchip.com/downloads/en/AppNotes/01494A.pdf.

[39] Nexperia. *BAV99 series - High-speed switching diodes*. Nov. 2010. URL: https://assets.nexperia.com/documents/data_sheet/BAV99_SER.pdf.

[40] Vishay Semiconductors. *TEMD1000, TEMD1020, TEMD1030, TEMD1040 Silicon PIN Photodiode*. Aug. 2011. URL: https://www.vishay.com/doc?81564.

[41] OSRAM Opto Semiconductors GmbH. *SFH 4045N High Power Infrared Emitter (940 nm), Version 1.4*. Dec. 2015. URL: https://www.osram.com/media/resource/hires/osram-dam-2496064/SFH%204045N.pdf.